

• Original Paper •

Charney's Model—the Renowned Prototype of Baroclinic Instability—Is Barotropically Unstable As Well

Yuan-Bing ZHAO¹ and X. San LIANG*^{1,2,3}¹*School of Atmospheric Sciences, Nanjing University of Information Science and Technology, Nanjing 210044, China*²*School of Marine Sciences, Nanjing University of Information Science and Technology, Nanjing 210044, China*³*School of Mathematics and Statistics, Nanjing University of Information Science and Technology, Nanjing 210044, China*

(Received 7 September 2018; revised 16 February 2019; accepted 25 February 2019)

ABSTRACT

The Charney model is reexamined using a new mathematical tool, the multiscale window transform (MWT), and the MWT-based localized multiscale energetics analysis developed by Liang and Robinson to deal with realistic geophysical fluid flow processes. Traditionally, though this model has been taken as a prototype of baroclinic instability, it actually undergoes a mixed one. While baroclinic instability explains the bottom-trapped feature of the perturbation, the second extreme center in the perturbation field can only be explained by a new barotropic instability when the Charney–Green number $\gamma \ll 1$, which takes place throughout the fluid column, and is maximized at a height where its baroclinic counterpart stops functioning. The giving way of the baroclinic instability to a barotropic one at this height corresponds well to the rectification of the tilting found on the maps of perturbation velocity and pressure. Also established in this study is the relative importance of barotropic instability to baroclinic instability in terms of γ . When $\gamma \gg 1$, barotropic instability is negligible and hence the system can be viewed as purely baroclinic; when $\gamma \ll 1$, however, barotropic and baroclinic instabilities are of the same order; in fact, barotropic instability can be even stronger. The implication of these results has been discussed in linking them to real atmospheric processes.

Key words: Charney's model, multiscale window transform, canonical transfer, baroclinic instability, barotropic instability

Citation: Zhao, Y.-B., and X. S. Liang, 2019: Charney's model—the renowned prototype of baroclinic instability—is barotropically unstable as well. *Adv. Atmos. Sci.*, **36**(7), 733–752, <https://doi.org/10.1007/s00376-019-8189-8>.

Article Highlights:

- The Charney model actually has a flow system that is barotropically unstable as well.
- The relative importance of barotropic instability to baroclinic instability varies with the Charney–Green number (γ).
- The second maximum on the perturbation fields can only be explained by the barotropic instability when $\gamma \ll 1$.

1. Introduction

The Charney model (Charney, 1947) as a prototype of baroclinic instability has been extensively studied. The resulting perturbation patterns, though idealized, have been utilized to interpret the generation of midlatitude synoptic disturbances, such as those in frontal dynamics, storm track dynamics (e.g., Blackmon et al., 1977; Hoskins and Valdes, 1990; Nakamura, 1992; Chang and Orlanski, 1993), and so forth. Even today, this seemingly very old field is still active (Badin, 2014; Chai and Vallis, 2014). As noted by Pierrehumbert and Swanson (1995), “Baroclinic instability is far from a closed book, even in very classic areas.” Indeed, there are still questions unanswered with this model. For instance,

though most of the perturbation fields for an unstable mode are bottom-trapped, the vertical perturbation velocity w' is not, and, moreover, there exists a second extreme on the sectional distributions of the zonal perturbation flow u' and perturbation temperature T' (refer to section 3.3 in this study). How is this secondary center of the perturbation generated, and where is its energy from, if, in the classical point of view, the system undergoes a bottom-trapped baroclinic instability?

The only relevant explanation of the upper secondary maximum so far may come from the isentropic potential vorticity (PV) perspective. In the Charney model, the eastward propagating surface Rossby wave interacts with an internal Rossby wave, which lives on the background PV gradient and travels westward relative to the flow. The phases of these two counter-propagating Rossby waves must lock for exponential growth (Hoskins et al., 1985). Such an explanation is intuitive, but, more fundamentally, what behind the interaction is

* Corresponding author: X. S. LIANG
Email: x.san.liang@gmail.com

still unclear. A question first coming into mind is: how are the Rossby waves generated before the interaction, and where do the two waves receive energy for their growth?

On the other hand, it has long been overlooked that Charney's model admits instability processes that are local in nature. We know that, in the model, the interior PV gradient \bar{q}_y is positive, and so is the vertical shear at the lower boundary. This meets one of the four Charney–Stern–Pedlosky instability conditions (e.g., Vallis, 2006). However, such a condition is stated in a global sense, which does not imply a local instability structure. With regards to the Charney model, one often sees tilting patterns on the sectional distributions of perturbation fields. The westward tilting of the phase lines with height on the distributions of u' and p' (see section 3.3 below) is an indicator of baroclinic instability by the classical result. However, the phase variation with height is confined near the bottom. Over most of the fluid column the phase line is nearly straight (e.g., Charney, 1947; Kuo, 1952, 1979; Green, 1960; Geisler and Garcia, 1977; Fullmer, 1982; Branscome, 1983). Consequently, the heat flux via the unstable wave will be similarly confined to a region near the lower boundary.

Historically, multiscale energetics analysis has been used to infer the instability characteristics of the Charney model, since instabilities are essentially energy transfer processes between the mean and perturbation fields. Kuo (1952) argued that, in the Charney model, downward transport of zonal momentum $u'w'$ and northward heat transport $v'T'$ are important energy sources for perturbation kinetic energy. However, other studies (e.g., Green, 1960, 1970; Fullmer, 1982; Branscome, 1983; Pedlosky, 1987) have shown that the perturbation energy source in the Charney model is the potential energy (from the sloping isentropic surfaces) rather than the kinetic energy release of the vertical shear of the basic flow. On the other hand, although some of these features in the Charney model agree with those of more realistic atmosphere, major discrepancies exist between results derived from linear theory and observations. For instance, in the Charney model perturbation energy has only one maximum at the surface (Charney, 1947; Brown, 1969; Song, 1971; Simons, 1972), whereas in the real atmosphere there are two maxima in the vertical, one at the surface and the other near the tropopause, and the latter is in fact larger (e.g., Kao and Taylor, 1964; Lorenz, 1967). In some studies the formation of the upper-level maximum has been investigated with more realistic models (e.g., Simons, 1972; Gall, 1976a; Simmons and Hoskins, 1978), but few studies have ever been dedicated to explaining the secondary maximum at the upper levels of the Charney model. One possible reason may be because the maximum is unrealistically weak, whilst another may be due to the limitation of the methods available then. The above questions, though with a highly idealized model, actually appear to be difficult. The difficulty comes from the multiscale energetics, which form convenient diagnostic quantities for the problem, but do not have the needed local structure within the classical framework.

Ever since Lorenz (1955) set up a two-scale formalism of energetics with the Reynolds decomposition, ener-

getic analysis has become a powerful diagnostic tool for dynamic meteorology. This has been seen previously in studies of mean flow–wave/eddy interaction (e.g., Dickinson, 1969; Fels and Lindzen, 1973; Boyd, 1976; McWilliams and Restrepo, 1999), atmospheric blocking (Trenberth, 1986; Fournier, 2002), regional cyclogenesis (Cai and Mak, 1990), and storm tracks (e.g., Chang and Orlanski, 1993; Chapman et al., 2015), to name a few. This tool is particularly useful for the purpose of this study because the instability of a background flow is essentially a process that transfers energy from the background to perturbations. However, classical energetics, and the Lorenz cycle in particular, are stated in global form. That is to say, they are expressed in global averages or integrals (e.g., Pedlosky, 1987). In the past several decades, there has been a continuing effort to relax the spatial averaging/integration in order to extend this global formalism to regional atmospheric processes, for which averaged energetics may not yield useful information because of their localized nature (they tend to be locally defined in space and time and can be on the move). The instability that we will look in this study is such an example; it obviously has a vertical structure which will be disguised in a mean quantity diagnosis. The extension, of course, is by no means as trivial as a relaxation of the averaging/integration. The major issue here is how to separate the in-scale transport and the cross-scale transfer from the intertwined nonlinear process. A tradition started by Lorenz himself is to collect the terms in divergence form, and take them as the representation of the transport process. The remainder of the nonlinear interaction is then the energy transfer between the distinct scales (e.g., Harrison and Robinson, 1978).

The above approach to separating transport and transfer processes has been a standard practice in fluid dynamics research, particularly in turbulence research (cf. Pope, 2000). However, there is a severe issue to be resolved, as long pointed out by Holopainen (1978) and Plumb (1983) but mostly overlooked. While it is known that a transport process indeed bears a divergence form in the governing equations, the separation is not unique. Multiple divergence forms exist that may yield quite different transfers; that is to say, the so-obtained energy transfer in such an open system is quite ambiguous. This issue, which is actually quite profound in fluid dynamics, has long been identified but has not received enough attention, except for a few studies such as Plumb (1983). An early attempt to solve this problem is the multiscale energetics analysis by Liang and Robinson (2005), which is based on the multiscale window transform (MWT), a functional analysis tool that was later on rigorized (Liang and Anderson, 2007). However, in Liang and Robinson (2005), the transport–transfer separation was introduced in a half-empirical way. Recently, Liang (2016) found that this actually can be put on a rigorous footing. The energy transfer can be rigorously derived, and the resulting expression is unique. Moreover, it bears a Lie bracket form, reminiscent of the Poisson bracket in Hamiltonian mechanics. In this study, we use the MWT-based multiscale energetics method to re-examine the Charney model and, unexpectedly, find that this

model, which has been taken as a prototype of baroclinic instability, actually undergoes a mixed one; the second extreme center on the perturbation flow can be largely explained by the newly discovered barotropic instability, and the accompanied kinetic energy (or barotropic) transfer is mainly contributed from the vertical momentum flux.

The paper is organized as follows: In the next two sections, we briefly introduce the methodology and the Charney model. Followed is a description of the generation of the dataset needed for the study. In section 4, a detailed energetics analysis is presented. This work is summarized in section 5.

2. Localized multiscale energy and vorticity analysis

The research method for this study is the multiscale energetics part of the localized multiscale energy and vorticity analysis, or MS-EVA for short (cf. Liang and Robinson, 2005); also to be used is the MS-EVA-based theory of localized finite-amplitude baroclinic and barotropic instabilities (Liang and Robinson, 2007). This is a systematic line of work, involving ingredients from different disciplines such as mathematics and geophysical fluid dynamics. A comprehensive description is beyond the scope of this paper. In the following we present just a very brief introduction. The reader is referred to Liang (2016) for details, or, alternatively, to Liang and Wang (2018), section 2, for another short introduction but with more details furnished.

MS-EVA is based on a novel functional analysis tool called multiscale window transform (MWT; Liang and Anderson, 2007). With the MWT, one can split a function space into a direct sum of several mutually orthogonal subspaces, each with an exclusive range of time scales, while having its local properties preserved. Such a subspace is termed a “scale window”, or simply a “window”. A scale window is bounded above and below by two scale levels. In the M -window case, they are bounded above by M scale levels: j_0, j_1, \dots, j_{M-1} . (A level j corresponds to a period $2^{-j}\tau$ for a time duration τ .) For convenience, these windows will be denoted with $\varpi = 0, 1, \dots, M - 1$, respectively.

MWT can be viewed as a generalization of the classical Reynolds decomposition; originally it was developed to faithfully represent the energies (and any quadratic quantities) on the resulting scale windows. This is the key to multiscale energetics analysis. Liang and Anderson (2007) found that, for some specially constructed orthogonal filters, there exists a transfer-reconstruction pair, namely, MWT and its counterpart, multiscale window reconstruction (MWR), just like Fourier transform and inverse Fourier transform. In other words, MWR is just like a filter in the traditional sense. What makes it distinctly different is that, for each MWR, there exists an MWT which gives transform coefficients that can be used to represent the energy of the filtered series. (Normally, with a traditional filter there are no such coefficients and hence energy cannot even be represented; see below).

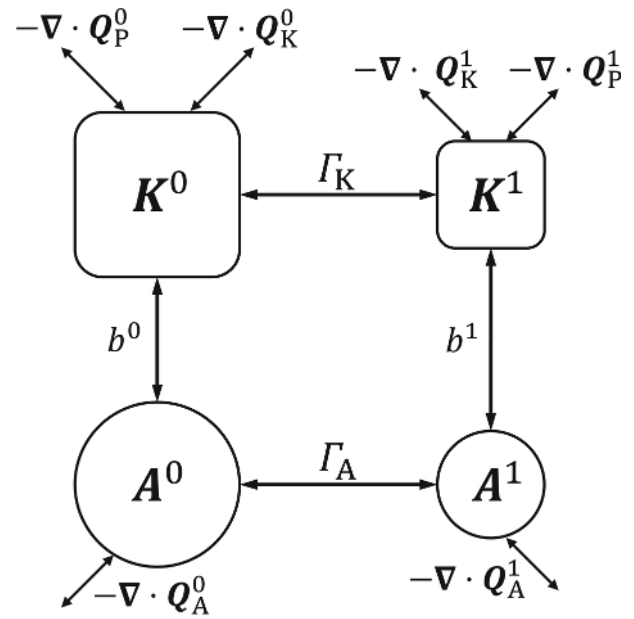


Fig. 1. Schematic illustration of the MS-EVA energetics for a two-scale window decomposition. The symbols are conventional in MS-EVA studies, with the superscripts 0 and 1 signifying the time-mean and perturbation windows, respectively. See Eqs. (8) and (9) and Table 1 for interpretations of the symbols.

Now, suppose $\{\varphi_n^j(t)\}_n$ is an orthonormal translational invariant scaling sequence [built from cubic splines; see Liang and Anderson (2007) and Fig. 1 in Liang (2016)], with j some scale level, n the time step, and t the time variable. Let $S(t)$ be some square integrable function defined on $[0, 1]$ (if not, the domain can always be rescaled to $[0, 1]$). Liang and Anderson (2007) showed that, in practice, all such functions can be expanded with $\{\varphi_n^j(t)\}_n$ as a basis; and the resulting transform,

$$\hat{S}_n^j = \int_0^1 S(t)\varphi_n^j(t)dt, \tag{1}$$

for any scale level j (corresponding to frequency 2^j), is called a scaling transform. Given window bounds j_0, j_1 for a two-window decomposition, S can then be reconstructed on the windows formed above:

$$S^{\sim 0}(t) = \sum_{n=0}^{2^{j_0}-1} \hat{S}_n^{j_0}\varphi_n^{j_0}(t), \tag{2}$$

$$S^{\sim 1}(t) = \sum_{n=0}^{2^{j_1}-1} \hat{S}_n^{j_1}\varphi_n^{j_1}(t) - S^{\sim 0}(t), \tag{3}$$

where $\sim 0, \sim 1$ indicate the corresponding scale windows. With these MWRs, the MWT of S is defined as

$$\hat{S}_n^{\sim \varpi} = \int_0^1 S^{\sim \varpi}(t)\varphi_n^{\sim \varpi}(t)dt, \tag{4}$$

for windows $\varpi = 0, 1$ and $n = 0, 1, \dots, 2^{j_1} - 1$. In terms of $\hat{S}_n^{\sim \varpi}$

the above MWRs can be written in one equation:

$$S^{\sim\varpi}(t) = \sum_{n=0}^{2^j-1} \hat{S}_n^{\sim\varpi} \varphi_n^{j_1}(t). \quad (5)$$

The two equations for $\hat{S}_n^{\sim\varpi}$ and $S^{\sim\varpi}(t)$ form a transform-reconstruction pair for the MWT. Note that the $S^{\sim\varpi}(t)$ are just like the low/high-pass filtered quantities which are defined in physical space, while the transform coefficients $\hat{S}_n^{\sim\varpi}$ (just like Fourier coefficients) can be used to represent multiscale energy—it has been rigorously proven that the energy on scale ϖ is precisely proportional to the square of the MWT coefficients (Liang and Anderson, 2007). For example, the perturbation energy extracted from $S(t)$ is simply $(\hat{S}_n^{\sim\varpi})^2$ multiplied by some constant. It is by no means the filtered quantities $(S^{\sim\varpi})^2$, which, however, has been frequently seen in the literature! Moreover, since $\hat{S}_n^{\sim\varpi}$ is localized (time location labeled by n), time variation can be spoken for the resulting energetics even though the multiscale decomposition is performed with respect to time, in contrast to the traditional Reynolds decomposition, which, if performed with respect to time, only results in time-invariant energetics.

With MWT, the available potential energy (APE) and kinetic energy (KE) densities (for convenience, we simply refer to them as APE and KE, unless confusion may arise) for window ϖ can be defined, following Lorenz (1955), as

$$A_n^{\varpi} = \frac{1}{2} \varrho (\widehat{T}_n^{\sim\varpi})^2, \quad (6)$$

$$K_n^{\varpi} = \frac{1}{2} \widehat{\mathbf{v}}_{h,n}^{\sim\varpi} \cdot \widehat{\mathbf{v}}_{h,n}^{\sim\varpi}. \quad (7)$$

In the above definitions, $\mathbf{v}_h = (u, v)$ is the horizontal velocity, T is the temperature anomaly [with the mean vertical profile $\overline{T}(z)$ removed], and ϱ is a proportionality depending on the buoyancy frequency. In the absence of diffusion/dissipation, the multiscale energy equations for a geophysical fluid system can now be symbolically written out (location n in the subscript omitted henceforth for simplicity):

$$\frac{\partial A^{\varpi}}{\partial t} = -\nabla \cdot \mathbf{Q}_A^{\varpi} + \Gamma_A^{\varpi} + b^{\varpi} + \mathfrak{C}_A^{\varpi}, \quad (8)$$

$$\frac{\partial K^{\varpi}}{\partial t} = -\nabla \cdot \mathbf{Q}_K^{\varpi} + \Gamma_K^{\varpi} - \nabla \cdot \mathbf{Q}_K^{\varpi} - b^{\varpi}, \quad (9)$$

for $\varpi = 0, 1$. The mathematical expressions and interpretations of the terms in Eqs. (8) and (9) are tabulated in Table 1; their names are the same as many others (e.g., Orlanski and Katzfey, 1991; Chang, 1993; Yin, 2002)^a. It should be noted that all terms are localized both in space and in time; in other words, they are all four-dimensional field variables, distinguished notably from the classical formalisms in which localization is lost in at least one dimension of space–time to achieve the scale decomposition. Processes intermittent in space and time are thus naturally embedded in Eqs. (8) and (9). Figure 1 schematizes the local Lorenz cycle with a two-window decomposition.

^aNote that the time tendency in Eqs. (8) and (9) in Charney's model is meaningless since the basic flow has been assumed to be steady. Nevertheless, it has nothing to do with the other terms in the energy equation, in which we are interested most.

Although the terms in Eqs. (8) and (9) have the traditional names, they are distinctly different from those in the traditional formalism. The most distinct terms are Γ_A^{ϖ} and Γ_K^{ϖ} . For a scalar field S within a flow $\mathbf{v} = (u, v, w)$, the energy transfer from other scale windows to window ϖ rigorously proves (Liang, 2016) to be (now the subscript n is supplied)

$$\Gamma_n^{\varpi} = -E_n^{\varpi} \nabla \cdot \mathbf{v}_S^{\varpi} = \frac{1}{2} [(\widehat{\mathbf{v}S})_n^{\sim\varpi} \cdot \nabla \hat{S}_n^{\sim\varpi} - \hat{S}_n^{\sim\varpi} \nabla \cdot (\widehat{\mathbf{v}S})_n^{\sim\varpi}], \quad (10)$$

where $E_n^{\varpi} = [\varrho (\hat{S}_n^{\sim\varpi})^2]/2$, with ϱ some constant, is the energy on window ϖ at step n [e.g., if S is the temperature anomaly, then E_n^{ϖ} is APE; refer to Liang (2016) for a detailed explanation], and

$$\mathbf{v}_S^{\varpi} = \frac{(\widehat{\mathbf{v}S})_n^{\sim\varpi}}{\hat{S}_n^{\sim\varpi}}, \quad (11)$$

is referred to as the S -coupled velocity. According to Eq. (10), Γ_n^{ϖ} has a Lie bracket form, reminding us of the Poisson bracket in Hamiltonian mechanics [a recent reference linking geophysical fluid dynamics (GFD) to Hamiltonian mechanics is referred to Badin and Crisciani (2018)]. It also possesses a very important property,

$$\sum_{\varpi} \sum_n \Gamma_n^{\varpi} = 0, \quad (12)$$

as first proposed in Liang and Robinson (2005) and later proved in Liang (2016). Physically, this implies that the transfer is a mere redistribution of energy among the scale windows, without generating or destroying energy as a whole. This property, though simple to state, does not hold in previous energetic formalisms (see below for a comparison to the classical formalism). To distinguish it from those that may have been encountered in the literature, it is termed “canonical transfer”.

Canonical transfer is fundamentally associated with energy conservation among scale windows during nonlinear interactions; this forms the key of the mode–mode interaction. That is to say, a mode may receive energy or lose energy to another mode, but on the whole energy should be conserved, as stated by Eq. (12). To further illustrate how canonical transfer differs from the classical formalism, in the following we consider a special case, i.e., a case with the traditional Reynolds decomposition. Since by Liang and Anderson (2007), MWT is a generalization of the Reynolds decomposition (i.e., the mean-eddy decomposition), we can specialize to consider this most particular case. Now, consider a passive tracer S in an incompressible flow, and neglect diffusion for simplicity:

$$\frac{\partial S}{\partial t} + \nabla \cdot (\mathbf{v}S) = 0. \quad (13)$$

Perform a Reynolds decomposition $S = \bar{S} + S'$ (with \bar{S} and S' respectively denoting the mean and perturbation), and the

Table 1. Mathematical expressions and physical interpretations for the energetics terms in Eqs. (8) and (9). The colon operator ($:$) in Γ_K^ω and Γ_A^ω is defined such that, for two dyadic products \mathbf{AB} and \mathbf{CD} , $(\mathbf{AB}) : (\mathbf{CD}) = (\mathbf{A} \cdot \mathbf{C})(\mathbf{B} \cdot \mathbf{D})$. For details, refer to Liang (2016).

Symbol	Mathematical expression	Physical interpretation
K^ω	$\frac{1}{2} \hat{\mathbf{v}}_h^{\sim\omega} \cdot \hat{\mathbf{v}}_h^{\sim\omega}$	KE on window ω
\mathcal{Q}_K^ω	$\frac{1}{2} (\widehat{\mathbf{v}\mathbf{v}_h})^{\sim\omega} \cdot \hat{\mathbf{v}}_h^{\sim\omega}$	Flux of KE on window ω
Γ_K^ω	$\frac{1}{2} [(\widehat{\mathbf{v}\mathbf{v}_h})^{\sim\omega} : \nabla \hat{\mathbf{v}}_h^{\sim\omega} - \nabla \cdot (\widehat{\mathbf{v}\mathbf{v}_h})^{\sim\omega} \cdot \hat{\mathbf{v}}_h^{\sim\omega}]$	Canonical transfer of KE to window ω
\mathcal{Q}_P^ω	$\frac{1}{\rho_0} \hat{\mathbf{v}}^{\sim\omega} \hat{p}^{\sim\omega}$	Pressure flux on window ω
b^ω	$-\frac{g}{T} \hat{w}^{\sim\omega} \hat{T}^{\sim\omega}$	Buoyancy conversion on window ω (defined as negative if the conversion is from APE to KE)
A^ω	$\frac{1}{2} \varrho (\hat{T}^{\sim\omega})^2, \varrho = \frac{g}{T(g/c_p - L)}$	APE on window ω
\mathcal{Q}_A^ω	$\frac{1}{2} \varrho \hat{T}^{\sim\omega} (\widehat{\mathbf{v}T})^{\sim\omega}$	Flux of APE on window ω
Γ_A^ω	$\frac{\varrho}{2} [(\widehat{\mathbf{v}T})^{\sim\omega} \cdot \nabla \hat{T}^{\sim\omega} - \hat{T}^{\sim\omega} \nabla \cdot (\widehat{\mathbf{v}T})^{\sim\omega}]$	Canonical transfer of APE to window ω
\mathcal{E}_A^ω	$\frac{1}{2} \hat{T}^{\sim\omega} (\widehat{wT})^{\sim\omega} \frac{\partial \varrho}{\partial z}$	APE generation due to the vertical variation of statistic stability (s) on window ω

evolutions of the mean energy and eddy energy (variance) can be shown to be (e.g., Pope, 2000):

$$\frac{\partial}{\partial t} \left(\frac{1}{2} \overline{S^2} \right) + \nabla \cdot \left(\frac{1}{2} \overline{\mathbf{v}S^2} \right) = -\overline{S} \nabla \cdot (\overline{\mathbf{v}'S'}), \quad (14)$$

$$\frac{\partial}{\partial t} \left(\frac{1}{2} \overline{S'^2} \right) + \nabla \cdot \left(\frac{1}{2} \overline{\mathbf{v}S'^2} \right) = -\overline{\mathbf{v}'S'} \cdot \nabla \overline{S}. \quad (15)$$

the terms in divergence form are generally understood as the transports of the mean and eddy energies, and those on the right-hand side as the respective energy transfers. The latter are usually used to explain the dynamical source of the mean flow–eddy interaction. Particularly, when S is a velocity component, the right-hand side of the eddy energy equation, $R = -\mathbf{v}'S' \cdot \nabla \overline{S}$, has been interpreted as the rate of energy extracted by Reynolds stress, or “Reynolds stress extraction” for short, against the mean field to fuel the eddy growth; in the context of turbulence research, it is also referred to as the “rate of the turbulence production” (Pope, 2000). It has also been extensively utilized in dynamic meteorology to explain phenomena such as cyclogenesis, eddy shedding, etc. However, Holopainen (1978) and Plumb (1983) found that the transport-transfer separation is not unique and hence the resulting transfer seems to be ambiguous. Moreover, the two energy equations do not, in general, sum to zero on the right-hand side. This is not what one would expect of an energy transfer, which by physical intuition should be a redistribution of energy among scale windows, and should not generate nor destroy energy as a whole.

With the MS-EVA formalism, these are not issues any more. In this special case, the energy equations in the form of Eqs. (8) or (9) become [see Liang (2016) for rigorous derivation; for a brief illustration, refer to the second section of

Liang and Wang (2018)]

$$\frac{\partial}{\partial t} \left(\frac{1}{2} \overline{S^2} \right) + \nabla \cdot \left(\frac{1}{2} \overline{\mathbf{v}S^2} + \frac{1}{2} \overline{S \mathbf{v}'S'} \right) = -\Gamma, \quad (16)$$

$$\frac{\partial}{\partial t} \left(\frac{1}{2} \overline{S'^2} \right) + \nabla \cdot \left(\frac{1}{2} \overline{\mathbf{v}S'^2} + \frac{1}{2} \overline{S \mathbf{v}'S'} \right) = \Gamma, \quad (17)$$

where

$$\Gamma = \frac{1}{2} [\overline{S} \nabla \cdot (\overline{\mathbf{v}'S'}) - \overline{\mathbf{v}'S'} \cdot \nabla \overline{S}]. \quad (18)$$

This is in sharp contrast to the traditional one: now, one can see that the right-hand side is balanced. This Γ is the “canonical transfer” in this special case. Previously, Liang and Robinson (2007) illustrated, for a benchmark hydrodynamic instability model (Kuo, 1949) whose instability structure is analytically known, the traditional Reynolds stress extraction R does not give the correct source of instability, while Γ does. We further remark that these equations result from the MWT-based multiscale energetics formalism, which are rigorously derived through reconstructing atom-like building blocks of multiscale transports [see Liang (2016)]; and they are unique. More specifically, if S is temperature T , then Γ is baroclinic canonical transfer (Γ_A),

$$\Gamma_A = \frac{\varrho}{2} [\overline{T} \nabla \cdot (\overline{\mathbf{v}'T'}) - \overline{\mathbf{v}'T'} \cdot \nabla \overline{T}], \quad (19a)$$

with ϱ a multiplier depending on the lapse rate (see Table 1); if S is velocity (say u or v), Γ is barotropic canonical transfer (Γ_K). With a background field $\overline{\mathbf{v}} = (\overline{u}(y, z), 0, 0)$, Γ_K boils down to, in terms of u and v ,

$$\Gamma_K = \frac{1}{2} [\overline{u} \nabla \cdot (\overline{\mathbf{v}'u'}) - \overline{\mathbf{v}'u'} \cdot \nabla \overline{u}]. \quad (19b)$$

From this formula, it can clearly be seen that, within a stratified baroclinic flow (as in the Charney model), perturbations

can also extract kinetic energy from the vertical shear of the basic flow.

It has been established that the canonical transfer terms ($\Gamma_A^{\overline{w}}$ and $\Gamma_K^{\overline{w}}$) in Eqs. (8) and (9) are very important. Particularly, the mean-to-eddy parts of them correspond precisely to the two important geophysical fluid flow processes, i.e., baroclinic instability and barotropic instability (Liang and Robinson, 2007); details are referred to a recent publication (Liang, 2016). For notational convenience, they are written as BC and BT, respectively. A set of criteria was then derived in Liang and Robinson (2007) for instability identification:

(1) A flow is locally unstable if $BC + BT > 0$, and vice versa;

(2) For an unstable system, if $BT > 0$ and $BC \leq 0$, the instability the system undergoes is barotropic;

(3) For an unstable system, if $BC > 0$ and $BC \leq 0$, then the instability is baroclinic; and

(4) If both BT and BC are positive, the system must be undergoing a mixed instability.

Because of their physical meanings, in the following we refer to BT and BC as barotropic transfer and baroclinic transfer, respectively.

We remark that the concept of barotropic and baroclinic instabilities here is in the classical sense (e.g., Pedlosky, 1987): a flow is baroclinically (barotropically) unstable if potential (kinetic) energy is the only form of energy transferred from the mean flow to perturbation fields. However, the energy transfer terms used to infer instabilities, as denoted by BC and BT, are different from the traditional ones. In Eq. (7b), on spatial integration the first term (in a divergence form) on the right-hand side vanishes, whereas the second term $-\overline{v'u'} \cdot \nabla \bar{u}$ does not. The second term can be further divided into two parts: $-\overline{u'v'} \partial \bar{u} / \partial y$ and $-\overline{u'w'} \partial \bar{u} / \partial z$. In the case of quasi-geostrophic flow, because w vanishes to the first order, the kinetic energy transfer related to the vertical shear, $-\overline{u'w'} \partial \bar{u} / \partial z$, is zero. (In fact, because of this, barotropic instability is conventionally believed to be related only to the horizontal shear of the mean flow). But, it cannot be totally ignored. When localized instability is considered, it may appear significant locally, though globally it is still very small. Moreover, in some limiting cases, it could be significant. These are indeed what we will find soon in the Charney model (see below).

3. A brief review of the Charney model

3.1. Basic state

The Charney model talks about the instability of a constant shear flow in a stratified, semi-infinite atmosphere on a β -plane to quasi-geostrophic perturbations. The mean state (denoted by an overbar) of the Charney model therefore assumes

$$\bar{u} = \Lambda z, \quad \bar{v} = 0, \quad \bar{w} = 0, \quad (20)$$

where Λ is a constant. The mean temperature field (\bar{T}) and mean density ($\bar{\rho}$) are determined by the thermal wind relation

$$-\frac{1}{\bar{T}} \frac{\partial \bar{T}}{\partial y} = \frac{f\bar{u}}{g} \left(-\frac{1}{\bar{T}} \frac{\partial \bar{T}}{\partial z} + \frac{1}{\bar{u}} \frac{\partial \bar{u}}{\partial z} \right). \quad (21)$$

With \bar{T} and $\bar{\rho}$, the mean pressure field (\bar{p}) is obtained accordingly by the equation of state

$$\bar{p} = \bar{\rho} R \bar{T}. \quad (22)$$

The domain of the Charney model is semi-infinite with a solid flat bottom boundary. The boundary conditions are, therefore,

$$\bar{w} = 0, \quad z = 0, \quad (23a)$$

$$\bar{p} = 0, \quad z \rightarrow \infty. \quad (23b)$$

3.2. Eigenvalue problem

Charney's problem of baroclinic instability is governed by the linearized quasi-geostrophic PV equation (e.g., Charney, 1947; Kuo, 1952; Green, 1960; Burger, 1962; Miles, 1964; Lindzen and Farrell, 1980)

$$\left(\frac{\partial}{\partial t} + \bar{u} \frac{\partial}{\partial x} \right) q' + v' \hat{\beta} = 0, \quad (24)$$

where q' is the perturbation PV and $\hat{\beta} = \bar{q}_y$ is the meridional gradient of the background PV:

$$q' = \nabla^2 \Psi' + \frac{f_0^2}{\bar{\rho}} \frac{\partial}{\partial z} \left(\frac{\bar{\rho}}{N^2} \frac{\partial \Psi'}{\partial z} \right), \quad (25a)$$

$$\hat{\beta} = \beta - \frac{f_0^2}{\bar{\rho}} \frac{\partial}{\partial z} \left(\frac{\bar{\rho}}{N^2} \frac{d\bar{u}}{dz} \right), \quad (25b)$$

with f_0 the Coriolis parameter at a fixed latitude, $\beta = f_y$, Ψ' , the perturbation streamfunction, and others are conventional. In the Charney model, the above two equations are simplified by assuming the buoyancy frequency N to be constant and $\bar{\rho} = \rho_0 e^{-z/H_\rho}$, with H_ρ being a density scale height, which is also a constant. Under these assumptions, Eqs. (25a) and (25b) can be simplified as

$$q' = \nabla^2 \Psi' + \frac{f_0^2}{N^2} \frac{\partial^2 \Psi'}{\partial z^2} - \frac{f_0^2}{H_\rho N^2} \frac{\partial \Psi'}{\partial z}, \quad (25c)$$

$$\hat{\beta} = \beta + \frac{f_0^2 \Lambda}{H_\rho N^2}. \quad (25d)$$

The boundary conditions are $w' = 0$ at the ground, i.e.,

$$\frac{\partial \Psi'}{\partial t} \frac{\partial \Psi'}{\partial z} - \Lambda \frac{\partial \Psi'}{\partial x} = 0, \quad z = 0, \quad (26a)$$

and

$$\Psi' \rightarrow 0, \quad z \rightarrow \infty. \quad (26b)$$

Following convention, we look for normal modal solutions of the form

$$\Psi' = \tilde{\Psi}(z) e^{ik(x-ct)+ily}, \quad (27)$$

where k and l are respectively the zonal and meridional wavenumber, and c is the complex phase velocity. Substitution of Eq. (27) into Eqs. (24) and (26) gives

$$\frac{d^2 \tilde{\Psi}}{dz^2} - \frac{1}{H_\rho} \frac{d\tilde{\Psi}}{dz} + \frac{N^2}{f_0^2} \left(\frac{\hat{\beta}}{\Lambda z - c} - K^2 \right) \tilde{\Psi} = 0, \quad (28a)$$

where $K^2 = k^2 + l^2$, and

$$c \frac{d\tilde{\Psi}}{dz} + \Lambda \tilde{\Psi} = 0, \quad z = 0, \quad (28b)$$

$$\tilde{\Psi} \rightarrow 0, \quad z \rightarrow \infty. \quad (28c)$$

These equations form an eigenvalue problem. Since Eq. (28a) has a non-constant coefficient, its analytical solution is not easy to obtain, but can be solved conveniently through numerical method.

As in Chai and Vallis (2014), we first non-dimensionalize Eqs. (28a)–(28c) using

$$z = H_\rho \hat{z}, \quad c = \Lambda H_\rho \hat{c}, \quad K = L_R^{-1} \hat{K}, \quad (29)$$

where hats denote nondimensional quantities, and the horizontal scale is the Rossby radius defined as $L_R = (NH_\rho)/f_0$. Equations (28a)–(28c) then become

$$\frac{d^2 \tilde{\Psi}}{d\hat{z}^2} - \frac{d\tilde{\Psi}}{d\hat{z}} + \left(\frac{1+\gamma}{\hat{z}-\hat{c}} - \hat{K}^2 \right) \tilde{\Psi} = 0, \quad (30a)$$

where $\gamma = (\beta L_R^2)/(H_\rho \Lambda)$, and

$$\hat{c} \frac{d\tilde{\Psi}}{d\hat{z}} + \tilde{\Psi} = 0, \quad \hat{z} = 0, \quad (30b)$$

$$\tilde{\Psi} \rightarrow 0, \quad \hat{z} \rightarrow \infty. \quad (30c)$$

The nondimensional parameter γ in Eq. (30a) is known as the Charney–Green number. It is the ratio of the scale height of the atmosphere H_ρ to the dynamic vertical scale $h = (f_0^2 \Lambda)/(\beta N^2)$ (Held, 1978). As we can see, all the information on the mean flow (shear, stratification, latitude, etc.) is absorbed into this single parameter. When $\gamma \ll 1$, the solution corresponds to the deep mode; whereas, when $\gamma \gg 1$, the solution approaches the shallow mode (e.g., Held, 1978; Branscome, 1983).

In this study, we restrict ourselves to midlatitude (say 45°N) waves, with f_0 and β fixed. The vertical shear Λ is independent of H_ρ and N , whereas the latter two parameters are

associated with each other through the thermal wind relation [Eq. (21)] and the equation of state [Eq. (22)]. For instance, when $H_\rho = 8800$ m, N is about 0.0138. That is to say, γ is only determined by two parameters, (H_ρ, Λ) or (H_ρ, N) . Here, we use H_ρ and Λ . Figure 2 shows the relation between H_ρ and N , and the distribution of γ on the (H_ρ, Λ) -plane. We see that the larger the H_ρ , the smaller the N ; and, if H_ρ is fixed, γ increases as Λ decreases, and vice versa. For convenience, we fix the scale height H_ρ and let Λ vary in order to investigate the influence of γ on the energetics. In this study, we choose $H_\rho = 8800$ m (other values, e.g., 8200 m and 9400 m, have also been checked, and the results are similar).

We remark that Nakamura (1992) has once discussed the effect of vertical shear on the structure of baroclinic waves. But the conclusion of this study is quite different from that of Nakamura (1992). According to Nakamura (1992), the vertical scale of baroclinic waves is inversely proportional to the vertical shear of the wind speed: $h \approx fL_x/(2\pi\sqrt{N^2 + (\partial\bar{u}/\partial z)^2})$. However, in the Charney model, both the vertical scale h and the wavelength L_x of the most unstable baroclinic wave are proportional to the vertical shear: $h = f^2\partial\bar{u}/\partial z/(\beta N^2)$ and $L_x = f\partial\bar{u}/\partial z/(\beta N) = Nh/f$ (Green, 1960; Held, 1978; Branscome, 1983). This means that stronger vertical shear corresponds to longer and deeper waves, as opposed to the conclusion of Nakamura (1992).

3.3. Most unstable modal solution

Without losing generality, let the meridional wavenumber $l = 0$. The most unstable mode therefore does not vary with y (e.g., Lindzen and Farrell, 1980). Theoretically, the model height is infinite. In practice, it is set to be finite but with enough high altitude ($50H_\rho$ in this study). Discretize Eqs. (30a)–(30c) in the vertical direction, and the resulting eigenvalue problem is solved through iteration.

Figure 3 shows the variations of the nondimensional wavenumber, growth rate and phase speed of the most unstable mode with γ . We see that the wavenumber increases with γ , whereas the growth rate and phase speed decrease with γ . [Note that the nondimensional maximum growth rate

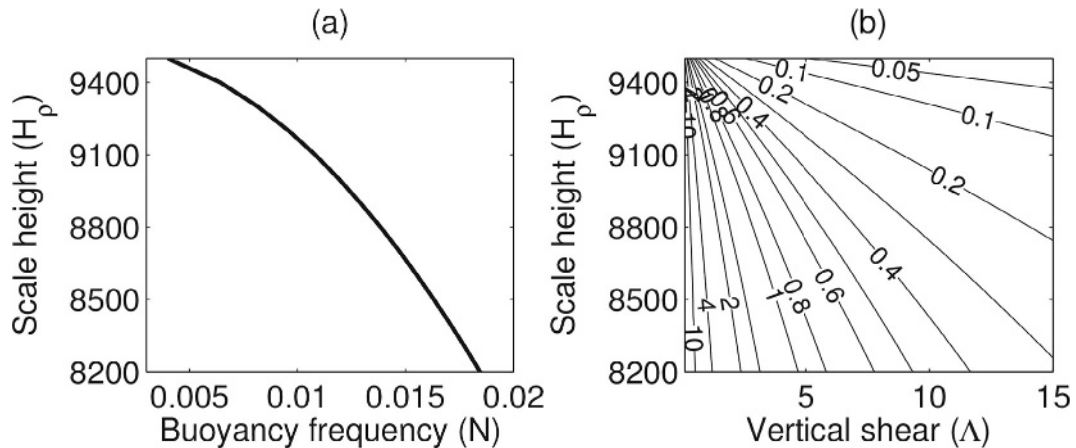


Fig. 2. (a) The relation between scale height H_ρ (meter) and buoyancy frequency N (s^{-1}). (b) Distribution of the Charney–Green number on the (H_ρ, Λ) -plane, where Λ is the vertical shear ($10^{-3} s^{-1}$).

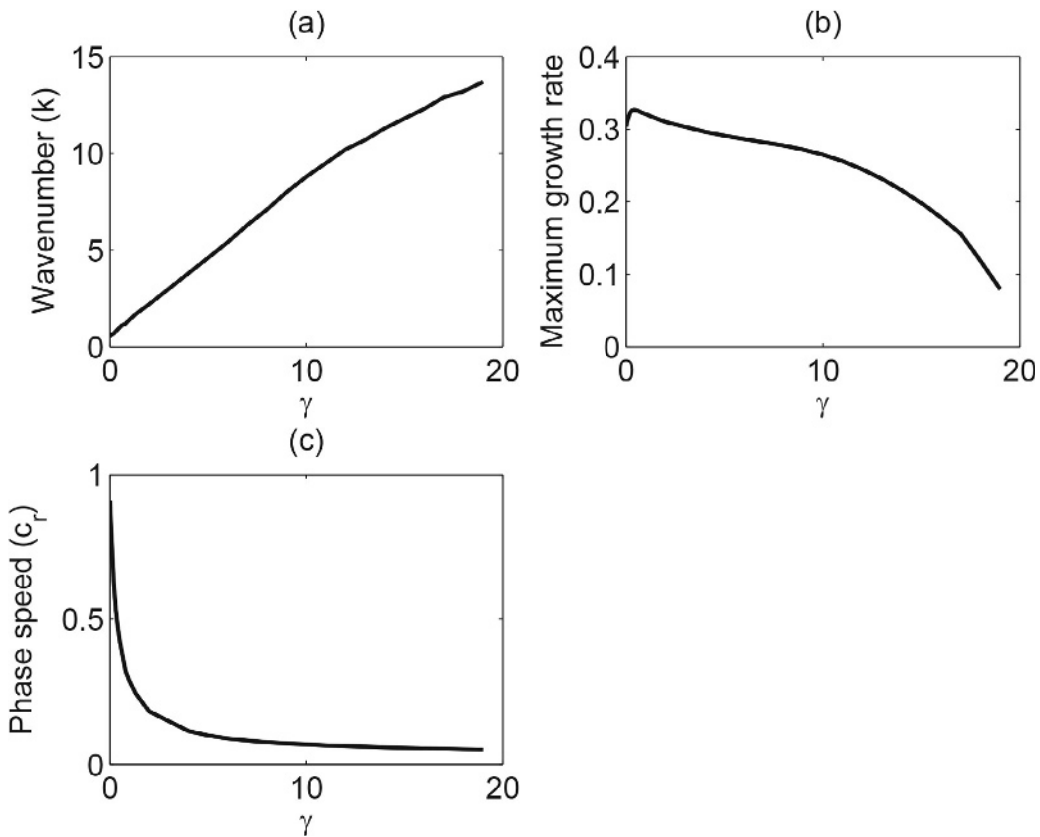


Fig. 3. Nondimensional (a) wavenumber (k), (b) maximum growth rate, and (c) phase speed (c_r) of the most unstable mode as a function of the Charney–Green number.

does not decrease monotonically, and it peaks at $\gamma = 0.4$ (Fig. 3b). But its dimensional counterpart [multiplied by $(f_0\Lambda)/N$] is monotonically decreasing with γ . This implies that a smaller γ corresponds to longer and deeper waves with larger growth rates and faster phase speeds. In particular, when $\gamma = 1.33$, the nondimensional wavenumber \hat{k} of the most unstable mode is 1.4, corresponding to the dimensional wavenumber $k = 1.4 \times 10^{-6} \text{ m}^{-1}$ and wavelength $L = 4504 \text{ km}$. And the corresponding nondimensional and dimensional growth rates are 0.3168 and 0.0175 hr^{-1} , respectively, implying that the wave amplitude will double in 40 hours. These results are consistent with previous studies, such as Kuo (1952, 1979), Gall (1976b), Lindzen and Farrell (1980), Farrell (1982), Chai and Vallis (2014), to name a few.

The perturbation fields of pressure, velocity and temperature are required, the solutions of which can be found from the literature (e.g., Kuo, 1952; Charney and Drazin, 1961; Gill, 1982). In nondimensional form, they are given by, respectively,

$$p' = \rho_0 f_0 \Psi', \tag{31a}$$

$$v' = \frac{if_0\hat{k}}{NH_\rho} \Psi', \tag{31b}$$

$$u' = -\frac{i}{N\hat{k}} \left\{ \left[\Lambda\hat{k}^2(\hat{z} - \hat{c}) - \frac{N^2 H_\rho}{f_0^2} \beta \right] v' - \Lambda \frac{dv'}{d\hat{z}} \right\}, \tag{31c}$$

$$w' = -\frac{f_0\Lambda}{N^2} \left[(\hat{z} - \hat{c}) \frac{dv'}{d\hat{z}} - v' \right], \tag{31d}$$

and

$$T' = -\frac{iNH_\rho}{\hat{k}} \left[\frac{v'}{R} + \frac{\bar{T}}{gH_\rho} \left(\frac{dv'}{d\hat{z}} - v' \right) \right]. \tag{31e}$$

Since Ψ' , the eigenvector, is already known, all the perturbation fields can now be determined.

The computed perturbation fields for the most unstable mode are shown in Fig. 4. Here, we show three typical cases: two extreme cases (the deep mode $\gamma = 0.1$ and the shallow mode $\gamma = 10$), and one moderate case ($\gamma = 1$). We can see that the wave structure varies with γ . Firstly, consistent with the analysis in the preceding parts, for $\gamma = 0.1$ the wave is long ($\sim 9L_R$) and deep (Figs. 4e–h), whereas for $\gamma = 10$ the wave is short ($\sim 0.7L_R$) and shallow (Figs. 4i–l). Secondly, the bottom trapping is stronger for larger γ . It can be seen that the upper-level centers for $\gamma = 0.1$ are more significant than those for $\gamma = 10$, especially in p' and u' . Thirdly, in the deep mode limit ($\gamma = 0.1$) the kinetic process dominates the thermal process (refer to the relative magnitude of u' and T'), whereas in the shallow mode limit ($\gamma = 10$) the relation reverses.

Apart from the major discrepancies described above, these three cases share much in common in terms of wave structure. Most conspicuous are the bottom-trapped feature in the distributions of p' (Figs. 4a, e and i) and T' (Figs. 4d, h and l), and the phase-line tilting with altitude, although the tilting varies from field to field. In the field of p' , the zero-isopleths have their greatest inclination in the lower levels

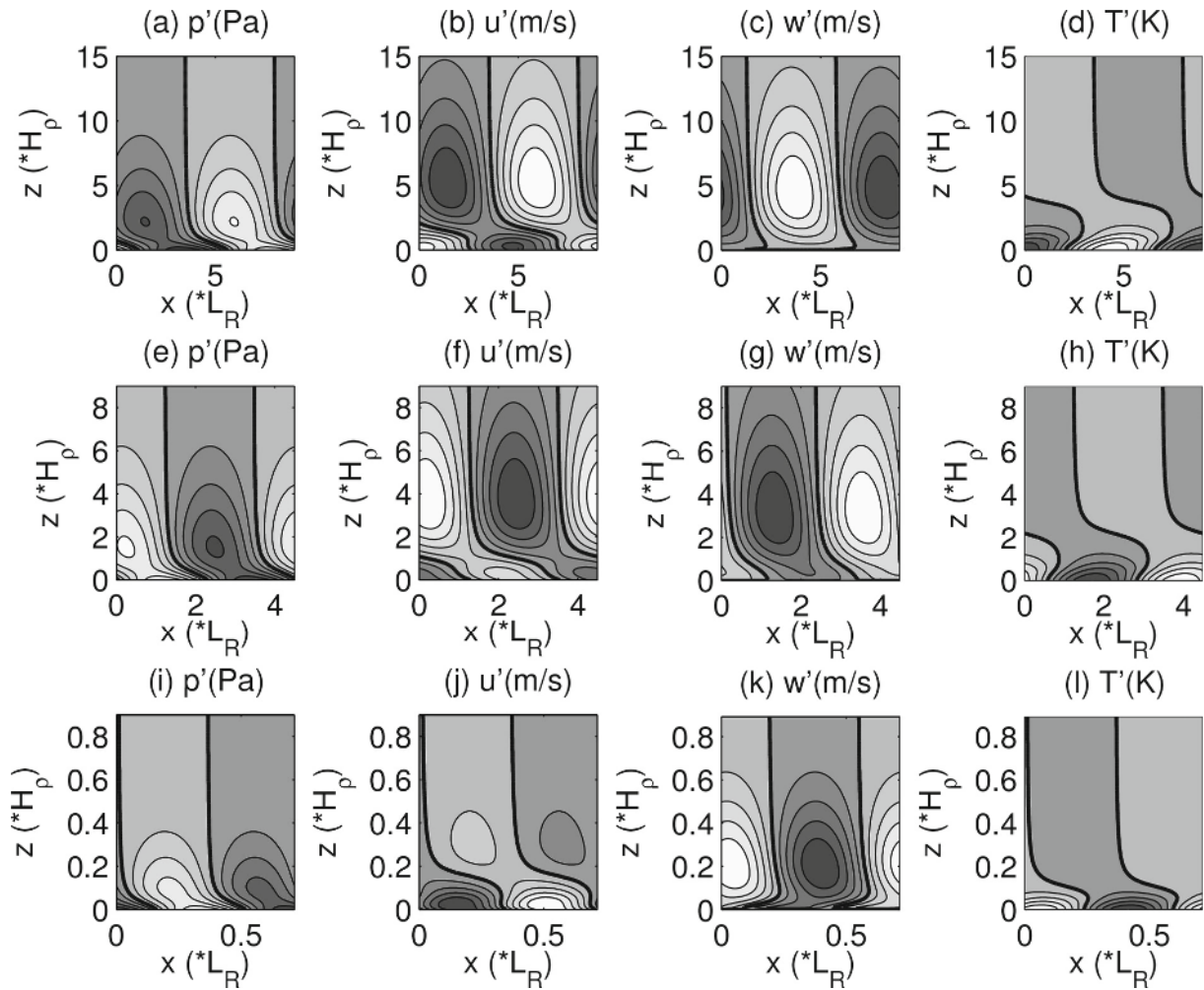


Fig. 4. Perturbation fields at the time instant when the maximal p' is taken to be 10 hPa at the surface: (a–d) $\gamma = 0.1$, (e–h) $\gamma = 1$, and (i–l) $\gamma = 10$. The field in each subplot has been normalized by its maximum. The scale height $H_\rho = 8800$ m, and the Rossby radius $L_R = 1218$ km.

and become nearly vertical in higher levels, as do the troughs and ridges. The phase difference is about $\pi/2$ through the vertical extent. The v' field (not shown) has a structure similar to p' , but with a phase lag of $\pi/2$. The fields of u' have two extreme centers vertically (Figs. 4b, f and j): one is at the bottom, and the other at upper levels. It can be seen that the zero-isopleths are nearly vertical at the bottom (except in Fig. 4f as $\gamma = 1$) and in the upper atmosphere, and tilt backward rapidly at lower levels. The phase lag between the upper layer and the bottom layer is from $2\pi/3$ to π . Distinctly different from u' and v' , the perturbation vertical velocity (Figs. 4c, g and k) attains its maximum value at middle-to-upper levels, with phase lines tilting slightly toward the west (except in Fig. 4k as $\gamma = 10$). The temperature has different inclinations in the lower layer and upper layer (Figs. 4d, h and l). It first tilts eastward in the bottom layer, then changes to the opposite direction in the middle layer, and becomes nearly vertical in the upper layer. This leads to the result that the phase of the upper layer ($2\pi/3 \sim \pi$) falls behind that in the lower layer. All these structures are consistent with previous studies (e.g., Charney, 1947; Kuo, 1952, 1979; Green, 1960; Gill, 1982;

Branscome, 1983).

4. MS-EVA analysis

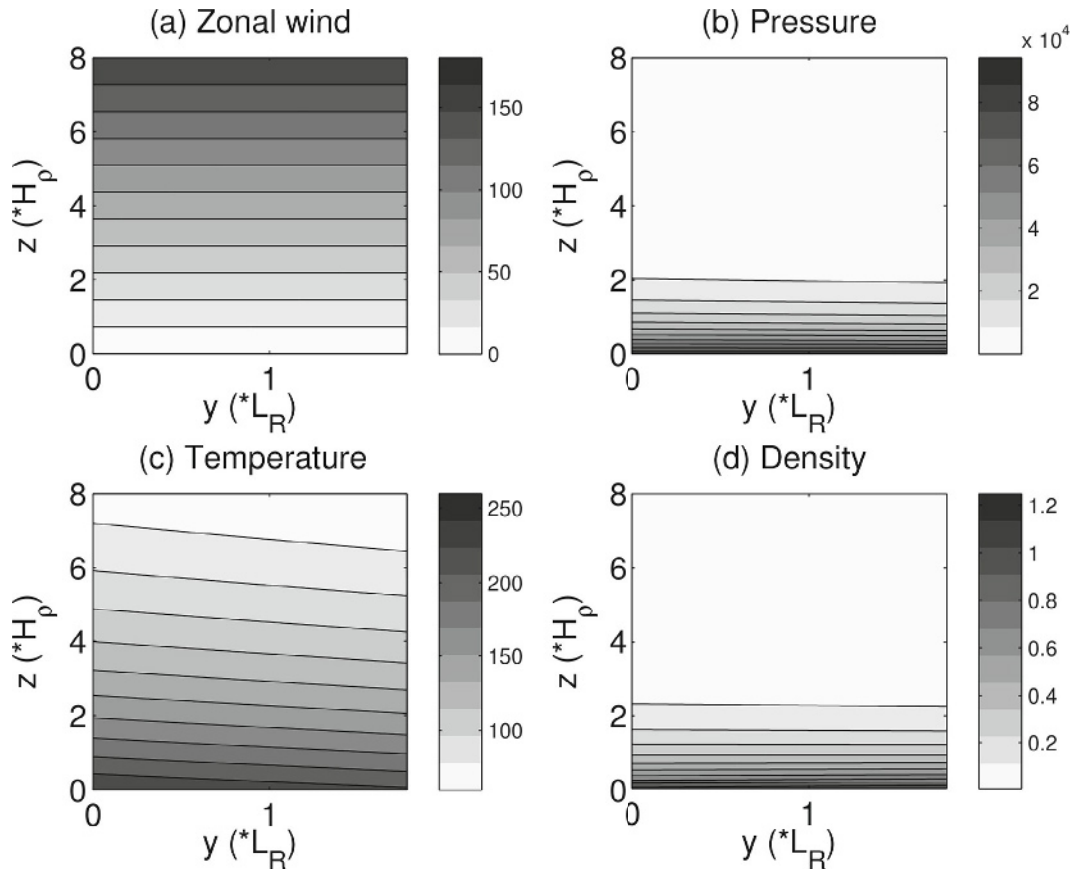
4.1. MS-EVA setup

The dataset obtained is in Cartesian coordinates. The series span four periods, which are divided into 2^8 time steps. In the x -direction the domain covers four wavelengths; it is discretized into 200 grid points. In the y -direction five grid points are chosen, with a spacing the same as Δx . In the vertical, 300 levels from bottom up are selected. Since what we are concerned with is the interaction between the basic state and the perturbations, the background-scale bound j_0 is chosen to be zero. In Liang and Anderson (2007), it was proven that this makes a field precisely its corresponding mean field.

For this study, three typical cases are chosen (refer to Fig. 4), i.e., two extreme cases (the deep mode limit $\gamma = 0.1$ and the shallow mode limit $\gamma = 10$) and a moderate case ($\gamma = 1$). The parameters of the corresponding mean flows are listed in Table 2. Given the values of these parameters, the mean fields

Table 2. Values of the key parameters of the mean states and the corresponding most unstable modes of the three selected cases.

	Parameters for the mean state			Information on the most unstable mode		
	β ($\text{m}^{-1} \text{s}^{-1}$)	H_ρ (m)	Λ (s^{-1})	Wavelength L (km)	Growth rate kc_i (hr^{-1})	Phase speed c_r (m s^{-1})
$\gamma = 0.1$	1.67×10^{-11}	8800	0.0282	10938	0.2312	185.64
$\gamma = 1.0$	—	—	2.80×10^{-3}	5469	0.0235	7.40
$\gamma = 10$	—	—	2.82×10^{-4}	890	0.0021	0.11

**Fig. 5.** Mean state of Charney's model as $\gamma = 1$: (a) zonal velocity (m s^{-1}); (b) pressure (Pa); (c) temperature (K); and (d) density (kg m^{-3}).

can be generated as shown in section 3.1. A reconstruction of the mean state of the Charney model as $\gamma = 1$ is shown in Fig. 5. Finally, the mean fields, together with the perturbation fields, form the input of MS-EVA.

4.2. Results analysis: $\gamma = 1$

4.2.1. Perturbation fields

With the datasets generated, a two-scale decomposition is performed for each field. To present the perturbation fields, we need only consider a particular instant. This is because, as a result of linearization, solutions of the Charney model are similar at all times, only with variations of magnitude and phase. Any snapshot of a field is typical of the evolution pattern of that field throughout the duration. Hereafter, we choose the time instant, at which the maximal value of p' on the surface is taken to be 10 hPa, to display the energetics. Moreover, as established by predecessors (and mentioned

before in this study), the most unstable mode corresponds to the y -wavenumber $l = 0$, which implies that the instability structure is y -independent. Therefore, only one x - z section is enough for the analysis.

The perturbation fields are expected to be reconstructed precisely on the perturbation-scale window; for example, p'^{-1} should be equal to p' , T'^{-1} should be T' , etc., and this is indeed true (not shown). The distributions of eddy (i.e., perturbation) APE (EAPE) and eddy kinetic energy (EKE), defined by Eqs. (1) and (2) as $\gamma = 1$, are shown in Fig. 6. Obviously, both EAPE and EKE are bottom-trapped. On the EAPE map (Fig. 6a), the trapping is especially strong, with most EAPE generally limited below the steering level ($0.3H_\rho$). Above that height, EAPE still exists, though in very small quantities; in fact, on the zonally averaged EAPE profile, above $1H_\rho$, there is a distinctly increasing trend with height (Fig. 6b). This feature seems to be odd but very robust (refer to the inset plot

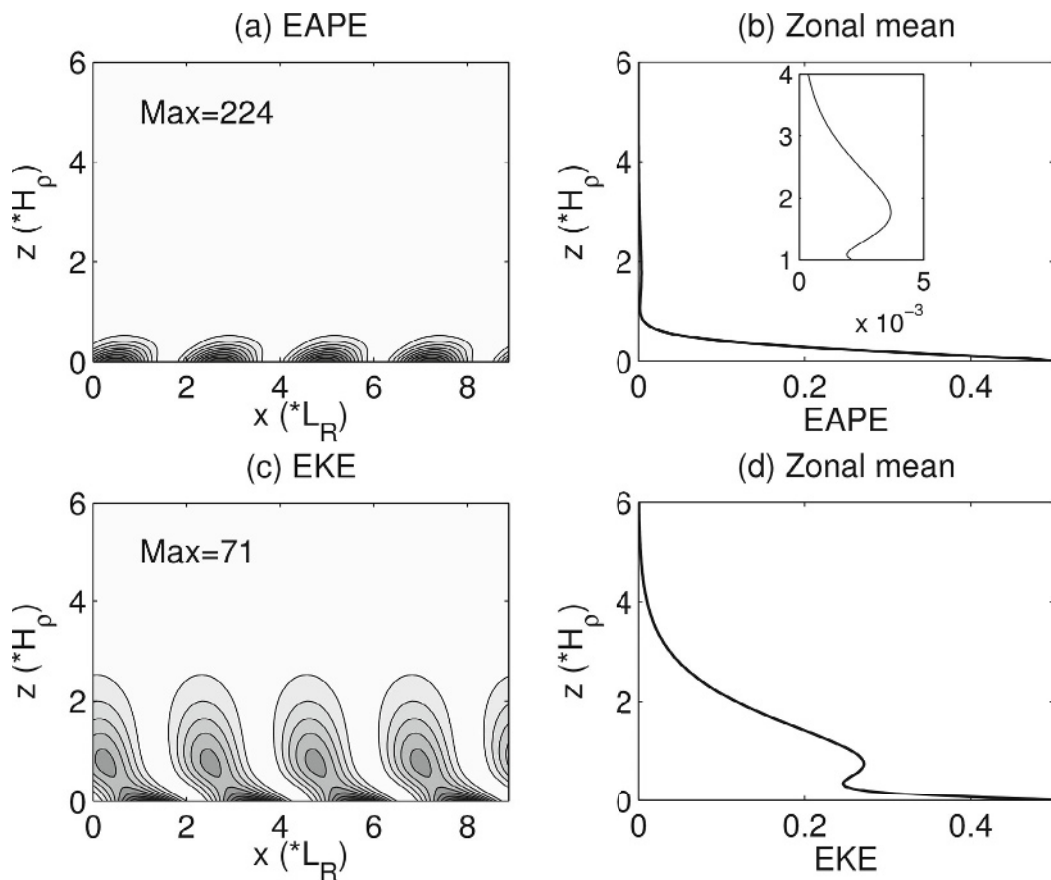


Fig. 6. EAPE ($\text{m}^2 \text{s}^{-2}$) and EKE ($\text{m}^2 \text{s}^{-2}$): (a) zonal section of EAPE; (b) zonal-mean EAPE; (c) zonal section of EKE; and (d) zonal-mean EKE.

in Fig. 6b). We shall get back to this point in the following subsection.

EKE is more colorful in structure (Fig. 6c). Apart from the bottom-trapping feature, the distribution has an appealing structure. Below $1H_\rho$, it tilts to the west with height; above that, it becomes almost vertical. Besides, a secondary maximum center occurs at around $1H_\rho$ where EAPE gets its minimum. This is more obvious in the zonally averaged profile (Fig. 6d). We discuss this further later in the paper.

4.2.2. *Baroclinic and barotropic canonical transfers*

The canonical transfers correspond precisely to the instabilities in geophysical fluid flows. We hence first look at these fields. Shown in Figs. 7a and b are the sectional distributions of the baroclinic transfer (BC) and its zonal average, respectively. Generally, it is positive below $2H_\rho$; that is to say, in the lower layer a baroclinic instability occurs, and the instability strength increases toward the bottom. Above $2H_\rho$, BC is even negative, though weak. In other words, the zonal flow within that layer is baroclinically stable.

The barotropic canonical transfer (BT) is by comparison two orders of magnitude smaller. What makes it merit particular attention is that it has a completely different structure (Figs. 7c and d). Its variation in the zonal direction is trapped in the middle layer. The zonal-mean BT takes its maximum at about $0.6H_\rho$, and vanishes at the top as well as the bottom.

Since it is positive throughout the vertical extent (except for the bottom), barotropic instability is occurring throughout the fluid column, but with an intensification in the middle and lower layers (between $0.5H_\rho$ and $3H_\rho$). Note that $1H_\rho$ is the height where BC tends toward zero. This explains why the tilting begins to inflect back at this height on the maps of u' and p' (Fig. 4), since the tilting signifies baroclinic instability but not barotropic instability.

The distribution of the total canonical transfer (BC plus BT) is quite similar to that for BC, especially in lower layers (below $1.5H_\rho$), as BT is very small compared to BC (Fig. 8a). Their difference occurs in the middle-to-upper layers. Above $1.5H_\rho$, BT can be many times larger than BC, which is negative (Fig. 8b). Together, they give a positive value. This means that the system is unstable, and the instability is mainly baroclinic. Besides, the baroclinic instability is bottom-trapped, agreeing with the traditional conclusion with the Charney model (e.g., Charney, 1947; Kuo, 1952; Green, 1960; Bretherton, 1966; Edmon et al., 1980). However, here, we find that the instability is not purely baroclinic. BT, though two orders of magnitude smaller, has a distinctly different structure. In fact, according to its formula (T_K) in section 2, the positive BT here is mainly a release of the kinetic energy of the vertical shear. As we will see soon below, it is this barotropic instability that causes the perturbation fields to deviate from a pure bottom-trapped pic-

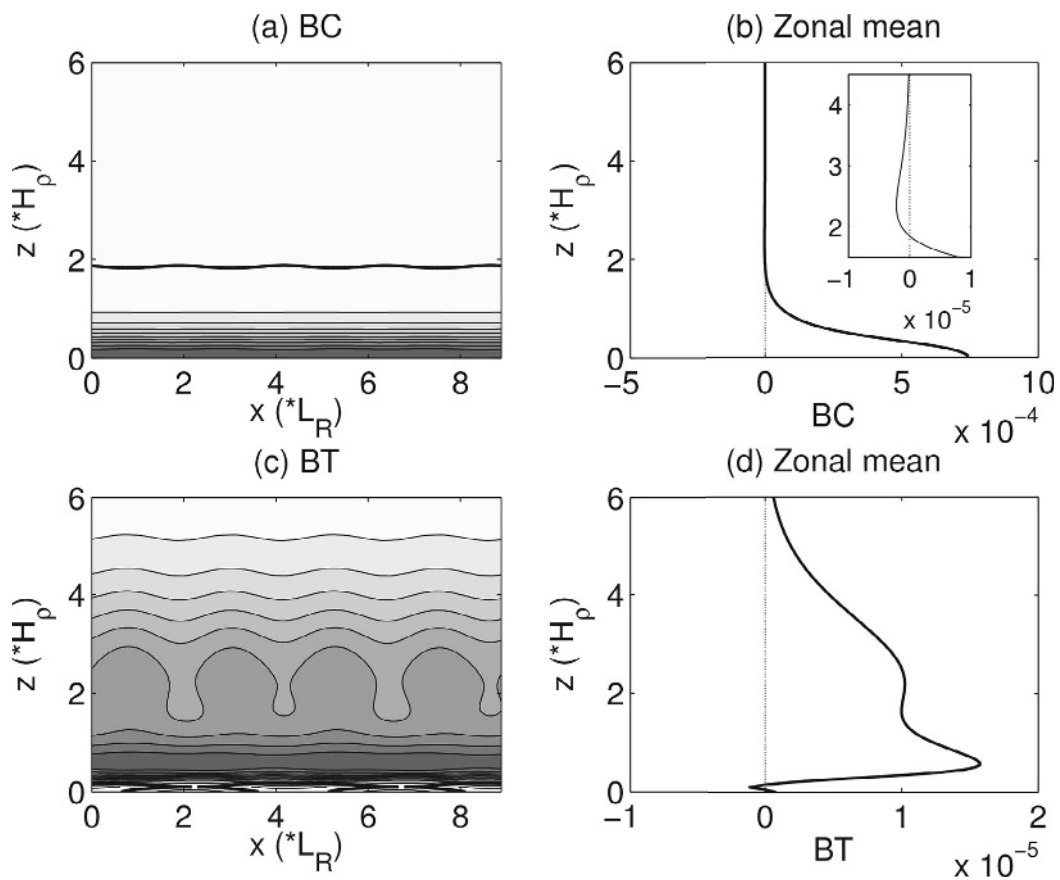


Fig. 7. BC ($\text{m}^2 \text{s}^{-3}$) and BT ($\text{m}^2 \text{s}^{-3}$): (a) zonal section of BC; (b) zonal-mean BC; (c) zonal section of BT; and (d) zonal-mean BT.

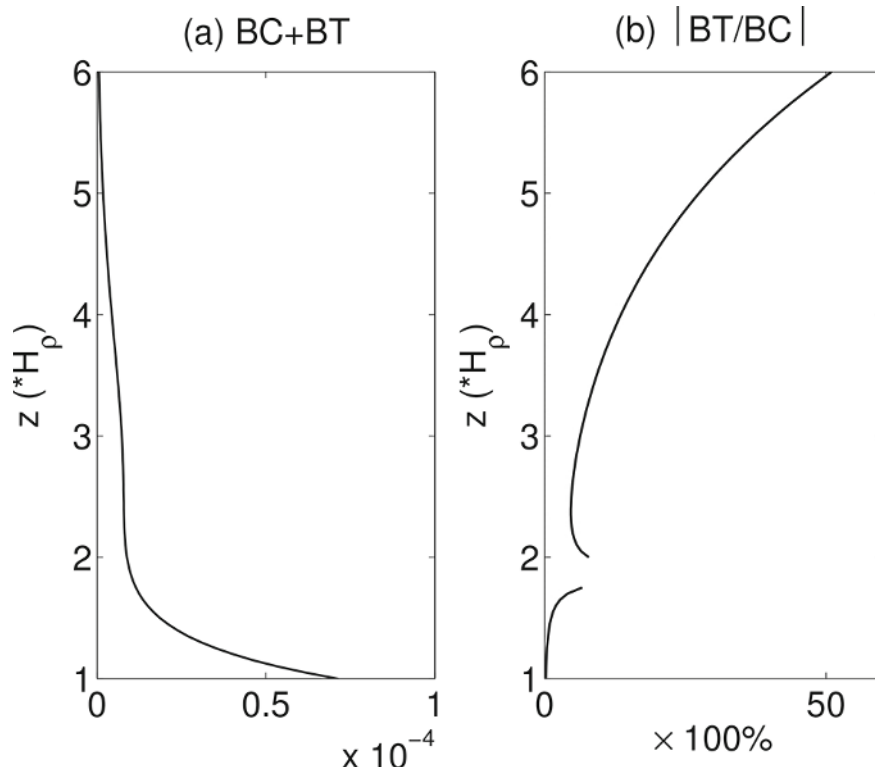


Fig. 8. Vertical profiles of (a) the total energy transfer (BC plus BT), and (b) the ratio of BC and BT. Note that the gap around $z = 2H_\rho$ in (b) is left intentionally since BC is almost zero there.

ture. Therefore, strictly speaking, the system is undergoing a mixed instability.

4.2.3. *Multiscale energy balance*

The canonical transfers allow us to reconstruct the instability structures. One would expect that they can explain the particular distributions of the perturbation energies. This is, however, not completely true here. Comparing Fig. 7 to Fig. 6, it is apparent that BC is negative above $2H_\rho$, while EAPE does not vanish there. Instead, a secondary EAPE center occurs there. One would naturally ask how the system gains its APE where there is no baroclinic instability at all. In the following, this, together with other issues, is addressed through a detailed analysis of the MS-EVA terms.

We first look at the perturbation buoyancy conversion (b^1). Buoyancy conversion is important in that it mediates between KE and APE and, in fact, is the only connection between KE and APE. It is an important process in the atmosphere and ocean, which also exists in quasi-geostrophic movements. Moreover, there are many studies concerning the buoyancy conversion process in idealized quasi-geostrophic models, such as Green (1960, 1970), Gall (1976b), Lapeyre and Klein (2006), Ragone and Badin (2016), etc. Drawn in Figs. 9a and b are, respectively, the sectional distribution of b^1 and its zonal average. A conspicuous feature is, again, the bottom-trapped negative conversion, i.e., the conversion from EAPE to EKE, with a maximum (in magnitude) taking place around $0.4H_\rho$ high. The conversion, however, reverses its direction at the upper levels. That is to say, now it becomes positive, though by comparison the conversion rate is much smaller. The critical height where the reversion takes place is about $2H_\rho$ (refer to the inset plot in Fig. 9b). A similar vertical structure of b^1 can be seen in previous studies, such as Green (1970), Gall (1976b), Branscome (1983), etc.

It should be pointed out that, besides the importance itself as a mechanism for energy to convert, buoyancy conversion has been extensively utilized in the literature for localized baroclinic instability studies (e.g., Gill, 1982). This is because of its localized nature, free of spatial averaging or integration, plus an intuitive argument that a negative buoyancy

conversion, i.e., a net conversion of EAPE to EKE, implies a baroclinic instability. While this may seem to be true sometimes, physically it is groundless. If one goes back to the fundamentals, one finds baroclinic instability and buoyancy conversion are two completely different concepts. They may correspond well on exceptional occasions, but generally the correspondence may not be seen, as has been evidenced in realistic problems (e.g., Zhao et al., 2016). In this problem, the maximal conversion (around $0.4H_\rho$) does not correspond to the maximal baroclinic instability (at the bottom), either.

Next, we look at the multiscale transport processes, i.e., which are represented by the \mathbf{Q} terms in the MS-EVA balance. Here, we have only these terms on the perturbation window. Plotted in Figs. 10a and c are the horizontal ($-\nabla \cdot \mathbf{Q}_{A,h}^1$) and vertical ($-\nabla \cdot \mathbf{Q}_{A,z}^1$) components of the EAPE flux convergence, respectively, and their corresponding zonal averages (Figs. 10b and d). The zonally averaged $-\nabla \cdot \mathbf{Q}_{A,h}^1$ is zero throughout the whole depth. This implies that EAPE is transported horizontally without its vertical distribution being changed, whereas another mechanism—namely, the vertical flux—is mainly to transport EAPE from the middle layer (between $0.3H_\rho$ and $1.2H_\rho$) to the bottom layer.

On the EKE, the transport processes could be due to both the convergence of EKE flux ($-\nabla \cdot \mathbf{Q}_K^1$) and the pressure flux ($-\nabla \cdot \mathbf{Q}_P^1$), either of which, as that for $-\nabla \cdot \mathbf{Q}_A^1$, has a horizontal component and a vertical component. Like $-\nabla \cdot \mathbf{Q}_{A,h}^1$, the zonal average of $-\nabla \cdot \mathbf{Q}_{K,h}^1$ is zero (Fig. 10f). For $-\nabla \cdot \mathbf{Q}_{K,z}^1$ (Fig. 10h), it is positive below $2H_\rho$ and negative above. Its maximum and minimum centers occur at $0.3H_\rho$ and $3H_\rho$, respectively. This implies that $-\nabla \cdot \mathbf{Q}_{K,z}^1$ contributes to the bottom trapping of EKE. Pressure working rate is quite differently, as shown in Figs. 10i-h. Firstly, both $-\nabla \cdot \mathbf{Q}_{P,h}^1$ and $-\nabla \cdot \mathbf{Q}_{P,z}^1$ tilt toward the west with height below $2H_\rho$, above which the phase line is almost vertical (Figs. 10i and k). Second, the zonal-mean profile of $-\nabla \cdot \mathbf{Q}_{P,h}^1$ almost vanishes (Fig. 10j), whereas $-\nabla \cdot \mathbf{Q}_{P,z}^1$ takes its minimum and maximum at $0.3H_\rho$ and $1.5H_\rho$, respectively, and begins to change sign at $1H_\rho$ (Fig. 10l). The vertical extent between $0.4H_\rho$ and $1.5H_\rho$ corresponds to the inflection region in the zonal-mean

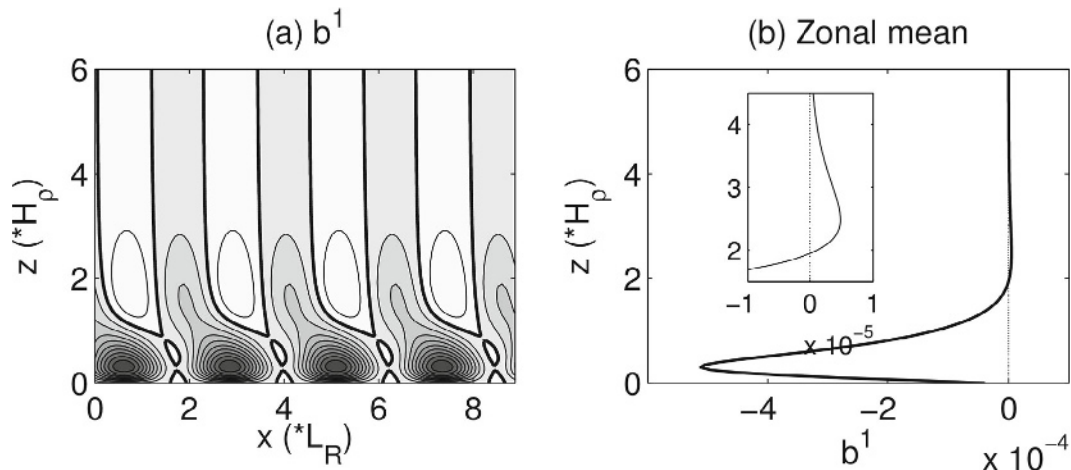


Fig. 9. (a) Zonal section of buoyancy conversion ($m^2 s^{-3}$), and (b) the zonal average.

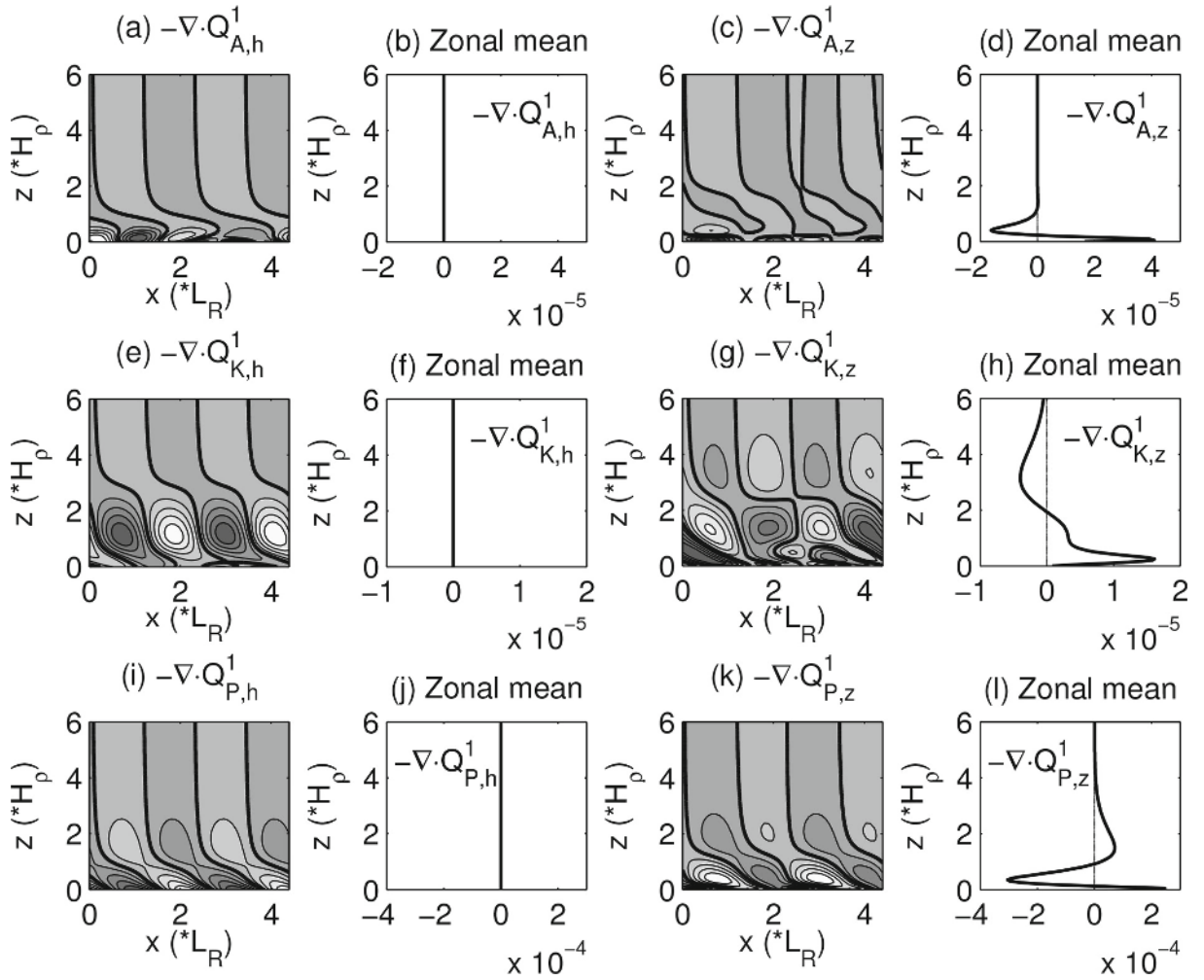


Fig. 10. (a–d) Horizontal and vertical EAPE flux convergences ($\text{m}^2 \text{s}^{-3}$): (a) zonal section of $-\nabla \cdot \mathbf{Q}_{A,h}^1$; (b) zonal-mean $-\nabla \cdot \mathbf{Q}_{A,h}^1$; (c) zonal section of $-\nabla \cdot \mathbf{Q}_{A,z}^1$; (d) zonal-mean $-\nabla \cdot \mathbf{Q}_{A,z}^1$. (e–h) As in (a–d), but for the EKE flux convergences ($-\nabla \cdot \mathbf{Q}_{K,h}^1$ and $-\nabla \cdot \mathbf{Q}_{K,z}^1$). (i–l) As in (a–d), but for pressure flux convergences ($-\nabla \cdot \mathbf{Q}_{P,h}^1$ and $-\nabla \cdot \mathbf{Q}_{P,z}^1$), respectively.

distribution of EKE (Fig. 6d).

From the above observations, the energetics scenario is now clear. We summarize it in Fig. 11. From the figure, the system is undergoing a baroclinic instability at the bottom, and most of the APE extracted at a height from the basic temperature field essentially remains at that height, causing T' fields to grow. T' is only horizontally transported through EAPE flux without their magnitudes changing; in contrast, EAPE is transported from the middle layer to the bottom through the vertical EAPE flux to fill the depletion of EAPE by buoyancy conversion. A part of EAPE is converted to EKE. The conversion takes place from the bottom through $2H_\rho$, and is maximized at $0.4H_\rho$. The converted energy at a level, however, does not remain at that level; rather, it is transported upward and downward through pressure flux. Consequently, EKE from the conversion is concentrated toward the bottom by $-\nabla \cdot \mathbf{Q}_{K,z}^1$. Besides, the unique vertical distribution of $-\nabla \cdot \mathbf{Q}_{P,z}^1$ causes the zonally averaged EKE profile to inflect between $0.4H_\rho$ and $1.5H_\rho$, and the secondary EKE center at $1H_\rho$. The scenario here is generally consistent with that de-

scribed by Gall (1976a).

On the other hand, the system also undergoes a barotropic instability, though much weaker. In contrast to the bottom trapping of its baroclinic counterpart, it takes place throughout the computational domain, intensified at middle-to-upper levels. This instability causes the system to extract energy from the background flow to fuel the perturbation flow, which makes the second extreme center in the field maps of u' (Fig. 4f) and the middle-level maximum of w' (Fig. 4g). The EKE, however, does not all go to the perturbation flow; a small part of it is converted into EAPE. This can be seen from the buoyancy map (Fig. 9b), which becomes positive above $2H_\rho$. In fact, this is the very reason why there is a small amount of EAPE in the upper domain (Fig. 6b), though there is no baroclinic instability there.

4.3. Results analysis: $\gamma = 0.1$ and $\gamma = 10$

4.3.1. Perturbation energy

Figure 12 shows the sectional distributions and vertical profiles of the two limiting cases. As we can see, in the deep

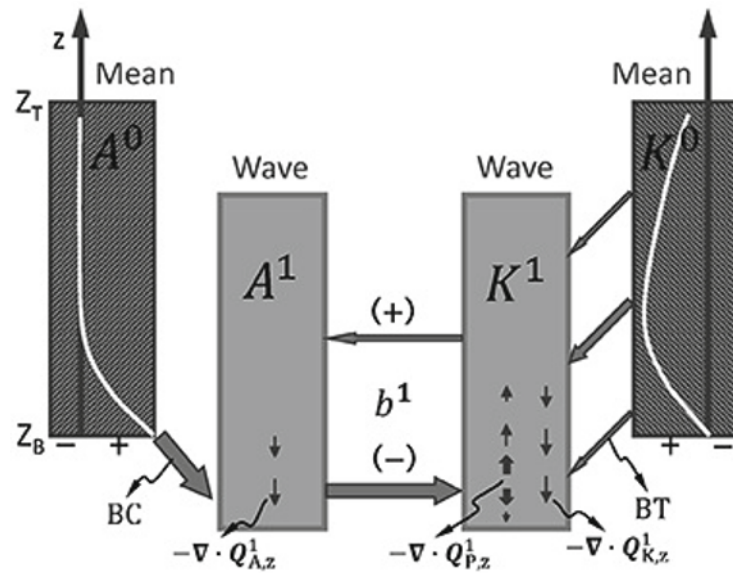


Fig. 11. Schematic illustration of the instability and energetics scenario in Charney's model as $\gamma = 1$. The small arrows in the diagram indicate the directions of various vertical transports (fluxes), with the width and length signifying the transport strength. Refer to the main text for details.

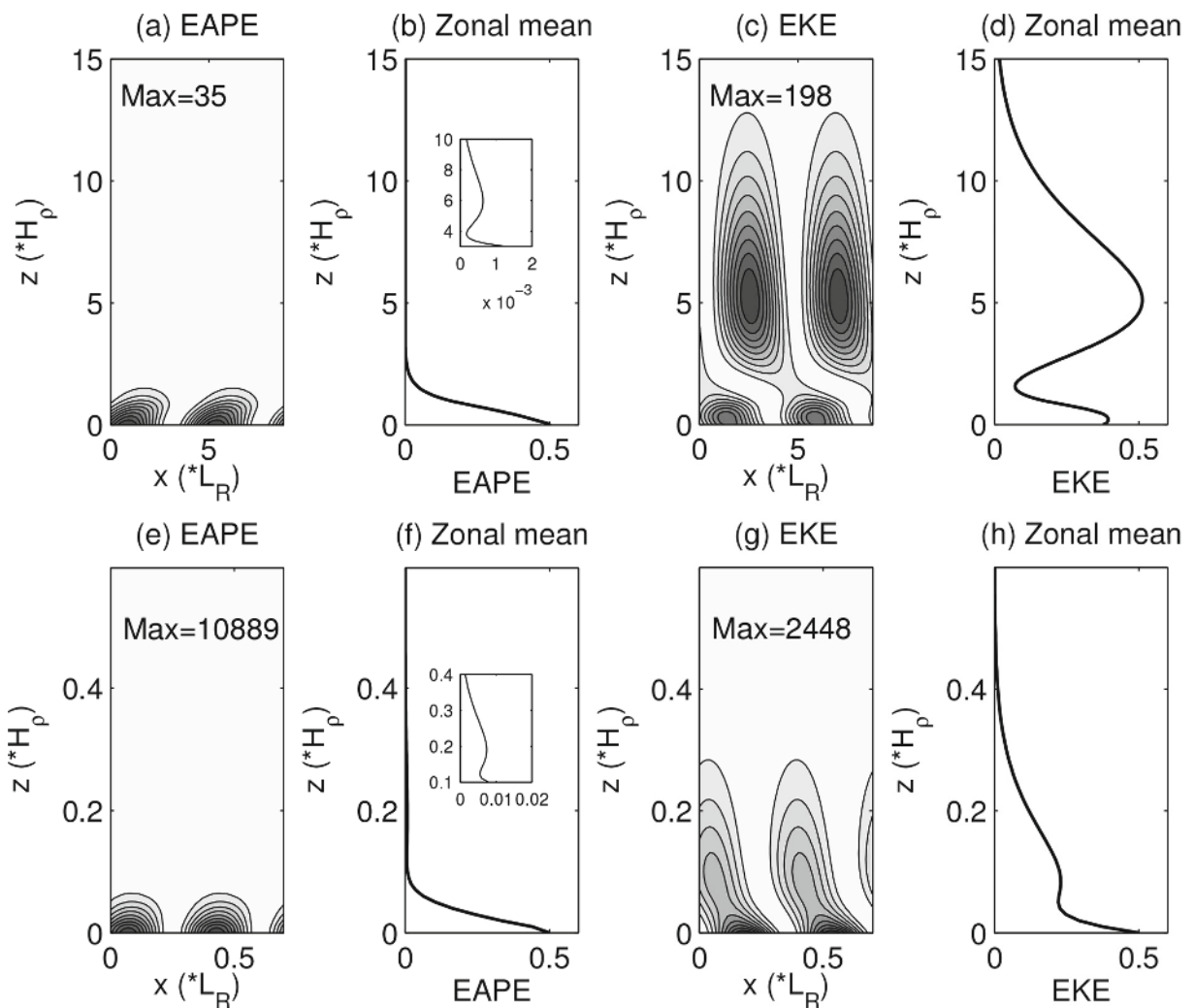


Fig. 12. As in Fig. 6, but for (a-d) $\gamma = 0.1$ and (e-h) $\gamma = 10$.

mode limit ($\gamma = 0.1$), EAPE is still bottom-trapped with a secondary maximum center at $6H_\rho$ (Fig. 12b), whereas the bottom trapping of EKE becomes moderate and its middle-level center at $5H_\rho$ is much stronger than its bottom counterpart (Fig. 12d). In the shallow mode limit ($\gamma = 10$), the bottom trapping intensifies. Both maximum centers of EAPE and EKE happen on the surface. Besides, the secondary EKE center weakens greatly (Fig. 12h), whereas that of EAPE at $0.2H_\rho$ is strengthened in a relative sense (Fig. 12f).

4.3.2. Canonical transfer

Figure 13 shows the vertical profiles of BC and BT of the two limiting cases. It is surprising to find that the relative importance of BC and BT varies with γ . In the deep mode limit, BC (Fig. 13a) and BT (Fig. 13b) have almost the same magnitude, with the latter even stronger than the former. BC is still bottom-trapped (below $5H_\rho$), but its maximum occurs above the surface rather than on it. BT is positive throughout the whole depth except at the bottom. Vertically, there are two maximum centers: one is at $1.5H_\rho$, and the other at $7H_\rho$. The upper-level center is much stronger than the lower one. On the contrary, in the shallow mode limit, BC (Fig. 13c) is four orders of magnitude larger than BT (Fig. 13d). Therefore, the system can be viewed as purely baroclinic. Note that in either these two limiting cases ($\gamma = 0.1$ and $\gamma = 10$) or the moderate case ($\gamma = 1$), BC is always negative in upper levels (Figs. 7b, 13a and 13c), indicating that the system is baroclinically

stable above a certain level.

4.3.3. Energy balance

The energetics balance also depends on γ . Figure 14 shows the vertical profiles of the zonally averaged b^1 , $-\nabla \cdot \mathbf{Q}_{A,z}^1$, $-\nabla \cdot \mathbf{Q}_{K,z}^1$, and $-\nabla \cdot \mathbf{Q}_{P,z}^1$. We can see that the structures are generally similar to those of $\gamma = 1$, but with a big difference in magnitude. For the deep mode, b^1 , $-\nabla \cdot \mathbf{Q}_{K,z}^1$ and $-\nabla \cdot \mathbf{Q}_{P,z}^1$ have the same magnitude, two orders larger than $-\nabla \cdot \mathbf{Q}_{A,z}^1$ (Fig. 14b). b^1 is negative below $7H_\rho$ and positive above (Fig. 14a). $-\nabla \cdot \mathbf{Q}_{K,z}^1$ is very strong and it has two maximum centers corresponding to that of EKE (Fig. 14c). Therefore, together with BC (Fig. 13a) and BT (Fig. 13b), the energy flow is that the perturbation obtains APE from the mean flow via baroclinic instability at low levels. Most of the EAPE is then converted to EKE through b^1 and the remaining part is transported downward by EAPE flux. Meanwhile, the flow is also undergoing a strong barotropic instability. The kinetic energy transfer from the mean flow to the perturbation mainly happens at upper levels. Then, EKE is transported via EKE flux and pressure flux to the lower levels. Therefore, the low-level EKE center benefits from both BC and BT, whereas the upper-level EKE center arises mainly from BT. In the upper layer, a small part of EKE is converted to EAPE, maintaining the secondary upper-level center in T' .

For the shallow mode, the perturbation energy is mainly

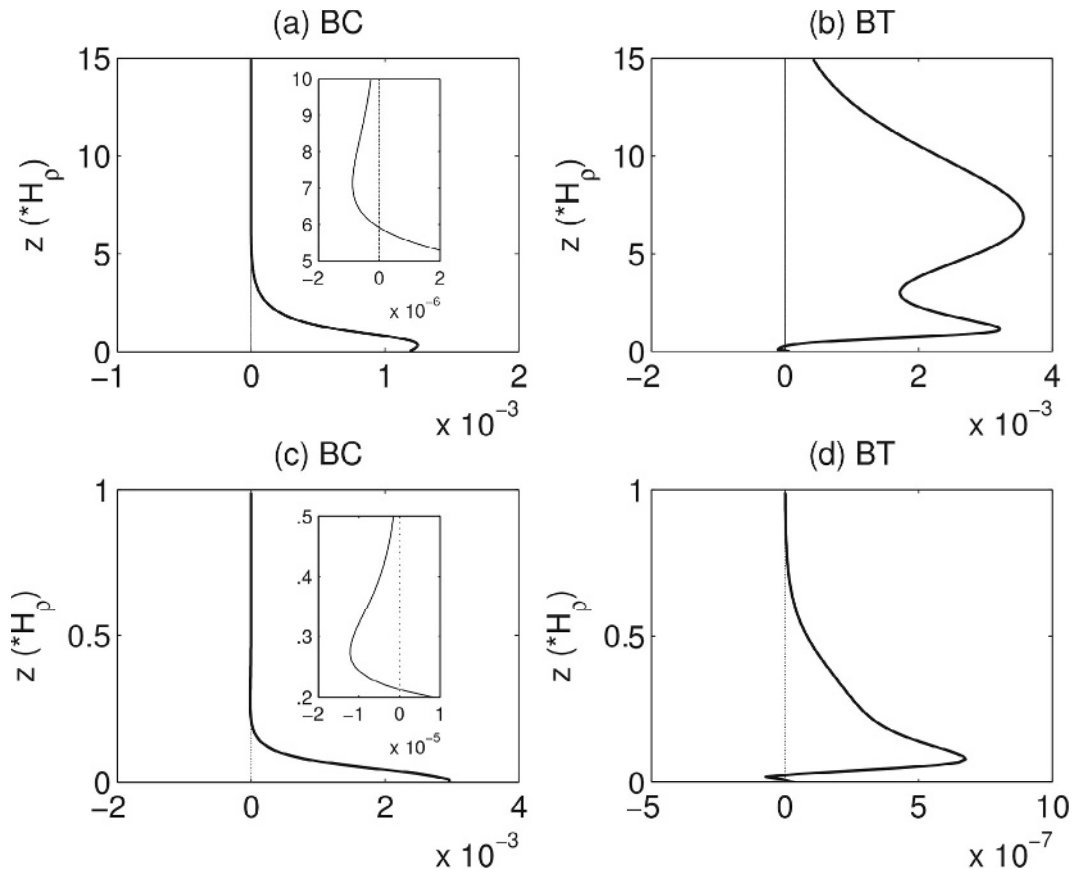


Fig. 13. Vertical profiles of zonal-mean (a, c) BC and (b, d) BT: (a, b) $\gamma = 0.1$; (c, d) $\gamma = 10$.

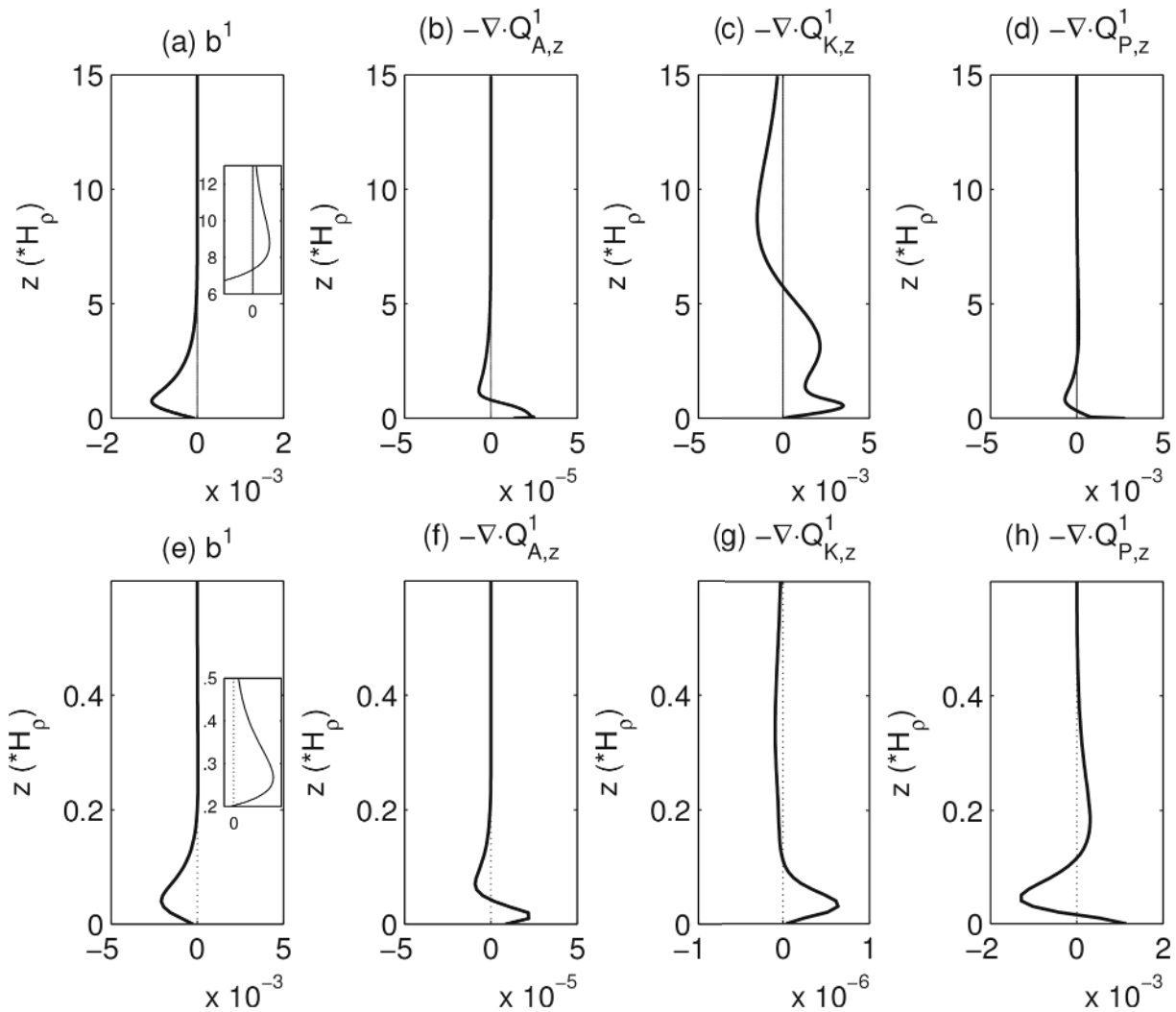


Fig. 14. As in Fig. 13, but for the conversion and transport terms: (a–d) $\gamma = 0.1$; (e–h) $\gamma = 10$.

balanced by three processes, i.e., BC (Fig. 13c), b^1 (Fig. 14e), and $-\nabla \cdot \mathbf{Q}_{P,z}^1$ (Fig. 14h), since BT (Fig. 13d), $-\nabla \cdot \mathbf{Q}_{A,z}^1$ (Fig. 14f), and $-\nabla \cdot \mathbf{Q}_{K,z}^1$ (Fig. 14g) are several orders of magnitude smaller. b^1 is negative and positive below and above $0.2H_\rho$, respectively (Fig. 14e). $-\nabla \cdot \mathbf{Q}_{P,z}^1$ is positive at the surface, negative in the lower layer, and positive at upper levels (Fig. 14h). The energy balance therefore becomes straightforward. The perturbation first obtains EAPE through BC in lower levels; then, part of it is converted to EKE; meanwhile, pressure flux transports EKE to the bottom and upper levels, which results in the secondary center on u' and p' ; at upper levels, EKE is converted back to EAPE, resulting in the secondary center in T' .

4.4. Correspondence in the real atmosphere

As presented above, we have found that the Charney model, which has been considered as a purely baroclinic model, actually also experiences barotropic instability processes. That is to say, apart from the energy from baroclinic canonical transfer, barotropic canonical transfer is also an

important source of energy for the most unstable Charney mode. This phenomenon has actually been observed in the real atmosphere. The waves over East Asia, which have been claimed to be of baroclinic origin, reveal similar behavior. Our recent study (Zhao et al., 2018) showed that these waves have two sources in East Asia: a northern one, which is located on the lee side of the Mongolian Plateau at middle and high latitudes; and a southern one, which generally coincides with the East Asian subtropical jet. MS-EVA diagnoses show that the waves in the southern branch experience strong baroclinic instability in the middle and lower layers, and strong barotropic instability in the upper layer; whereas, in the northern branch, the waves derive mainly from baroclinic instability [cf. Figs. 6 and 8 in Zhao et al. (2018)]. It is worth noting that the southern branch waves are located in the center of the jet stream, where the vertical shear is large, whereas in the north the vertical shear is small. These scenarios correspond qualitatively to the cases of $\gamma = 1$ and $\gamma = 10$, respectively, in this study.

It should be noted that, although the second maximum of the eddy energy in the upper levels in the Charney model can

correspond to the observed second peak of eddy activity near the tropopause (e.g., Kao and Taylor, 1964; Lorenz, 1967), they actually come from different mechanisms. As discussed above, the upper-level energy center in the Charney model is largely attributed to barotropic instability, whereas that observed near the tropopause is mainly due to buoyancy conversion and vertical transport of energy (e.g., Simons, 1972; Gall, 1976a; Simmons and Hoskins, 1978). Moreover, in the real extratropics, kinetic energy is mainly transferred from eddy to mean flow (e.g., Chang and Orlanski, 1993), which is opposite to that in the Charney model; and this process is mainly caused by the horizontal shear of the background flow (e.g., Deng and Mak, 2006; Zhao et al., 2018), whereas the Charney model does not at all have horizontal shear in the basic wind.

5. Conclusions

The Charney model is reinvestigated using the MS-EVA method developed by Liang and Robinson (2005) [see Liang (2016) for the updated version], which is based on a novel functional analysis tool—namely, the MWT (Liang and Anderson, 2007). For the first time, we are able to obtain a relatively complete instability structure, though this model as a prototype of baroclinic instability has been extensively studied before. Different from the traditional belief, the Charney model actually undergoes a mixed instability; that is to say, the instability is both baroclinic and barotropic, which are represented respectively by baroclinic canonical transfer (BC) and barotropic canonical transfer (BT) in the MS-EVA. The resulting BC has a vertical distribution agreeing with the traditional results, i.e., it is bottom-trapped, almost vanishing at the middle and upper levels. However, BC alone cannot explain why there exist temperature oscillations at the upper levels, and why there is a second extreme on the perturbation flow and pressure fields. Our study shows that a barotropic instability, though much weaker for most of the cases, actually exists throughout the fluid column. In the bottom region, it is overwhelmed by the baroclinic instability, but above that region where BC is small, its effect becomes significant. So, the instability is actually a mixed one. Besides, it is found that the relative importance of baroclinic instability and barotropic instability varies with the Charney–Green number γ , the ratio of atmosphere scale height H_p , and the perturbation vertical scale. In the shallow mode limit ($\gamma \gg 1$), barotropic instability is so weak that the system can be viewed as purely baroclinic. But, in the deep mode limit ($\gamma \ll 1$), barotropic instability is strong; in fact, it can be even stronger than baroclinic instability.

Accordingly, the energy balance and the maintenance of the upper-level centers in p' , u' , and T' in the Charney model also depend on γ . When $\gamma \gg 1$, BC is several orders of magnitude larger than BT. Therefore, the system can be viewed as purely baroclinic, and the energy source is BC only. The scenario of the energetics processes can be summarized as follows: First, the system receives EAPE through baroclinic

instability at the bottom. Then, most of the extracted APE goes to the perturbation temperature and causes it to grow, but a small part is converted into EKE, and the converted EKE is brought downward and upward through pressure flux, resulting in the bottom-trapped feature and the secondary centers in u' and p' . In the upper levels, a part of the EKE transported by pressure flux is converted to EAPE, leading to the formation of the secondary center in T' .

In contrast, for small γ , BC and BT are of the same order of magnitude. The energetics scenario is as follows: At the bottom, the system is undergoing a baroclinic instability. Most of the extracted APE goes to the perturbation temperature and causes it to grow, but a small part is converted into EKE, and the converted EKE is brought downward through pressure flux and EKE flux, making the perturbation flow fields become trapped at the bottom too. In the meantime, the system is also undergoing a barotropic instability, which becomes dominant at middle-to-upper levels, where the baroclinic instability stops functioning, and where the tilting on the maps of u' and p' becomes rectified. This explains why there is a second extreme center on the perturbation flow maps, and why EKE has an inflection on its vertical profile. Besides, a part of the EKE through the barotropic instability is converted to EAPE, providing the energy source for the observed oscillations of temperature at the upper heights, which, though identified long before, have been generally overlooked.

Acknowledgements. The suggestions of the two anonymous reviewers are appreciated. Yuan-Bing ZHAO thanks Yang YANG, Yi-Neng RONG, and Brandon J. BETHEL for their generous help. This research was supported by the National Science Foundation of China (Grant Nos. 41276032 and 41705024), the National Program on Global Change and Air–Sea Interaction (Grant No. GAS-IPOVAI-06), the Jiangsu Provincial Government through the 2015 Jiangsu Program of Entrepreneurship and Innovation Group and the Jiangsu Chair Professorship, and Shandong Meteorological Bureau (Contract No. QXPG20174023).

REFERENCES

- Badin, G., 2014: On the role of non-uniform stratification and short-wave instabilities in three-layer quasi-geostrophic turbulence. *Physics of Fluids*, **26**, 096603, <https://doi.org/10.1063/1.4895590>.
- Badin, G., and F. Crisciani, 2018: *Variational Formulation of Fluid and Geophysical Fluid Dynamics: Mechanics, Symmetries and Conservation Laws. Advances in Geophysical and Environmental Mechanics and Mathematics*, Springer, 182 pp, <https://doi.org/10.1007/978-3-319-59695-2>.
- Blackmon, M. L., J. M. Wallace, N.-C. Lau, and S. L. Mullen, 1977: An observational study of the northern hemisphere wintertime circulation. *J. Atmos. Sci.*, **34**, 1040–1053, [https://doi.org/10.1175/1520-0469\(1977\)034<1040:AOSOTN>2.0.CO;2](https://doi.org/10.1175/1520-0469(1977)034<1040:AOSOTN>2.0.CO;2).
- Boyd, J. P., 1976: The noninteraction of waves with the zonally averaged flow on a spherical earth and the interrelationships on eddy fluxes of energy, heat and momentum. *J. At-*

- mos. Sci.*, **33**, 2285–2291, [https://doi.org/10.1175/1520-0469\(1976\)033<2285:TNOWWT>2.0.CO;2](https://doi.org/10.1175/1520-0469(1976)033<2285:TNOWWT>2.0.CO;2).
- Branscome, L. E., 1983: The Charney Baroclinic stability problem: Approximate solutions and modal structures. *J. Atmos. Sci.*, **40**, 1393–1409, [https://doi.org/10.1175/1520-0469\(1983\)040<1393:TCBSPA>2.0.CO;2](https://doi.org/10.1175/1520-0469(1983)040<1393:TCBSPA>2.0.CO;2).
- Bretherton, F. P., 1966: Critical layer instability in baroclinic flows. *Quart. J. Roy. Meteor. Soc.*, **92**, 325–334, <https://doi.org/10.1002/qj.49709239302>.
- Brown, Jr. J. A., 1969: A numerical investigation of hydrodynamic instability and energy conversions in the quasi-geostrophic atmosphere: Part I. *J. Atmos. Sci.*, **26**, 352–365, [https://doi.org/10.1175/1520-0469\(1969\)026<0352:ANIOHI>2.0.CO;2](https://doi.org/10.1175/1520-0469(1969)026<0352:ANIOHI>2.0.CO;2).
- Burger, A. P., 1962: On the non-existence of critical wavelengths in a continuous baroclinic stability problem. *J. Atmos. Sci.*, **19**, 31–38, [https://doi.org/10.1175/1520-0469\(1962\)019<0031:OTNEOC>2.0.CO;2](https://doi.org/10.1175/1520-0469(1962)019<0031:OTNEOC>2.0.CO;2).
- Cai, M., and M. Mak, 1990: On the basic dynamics of regional cyclogenesis. *J. Atmos. Sci.*, **47**, 1417–1442, [https://doi.org/10.1175/1520-0469\(1990\)047<1417:OTBDOR>2.0.CO;2](https://doi.org/10.1175/1520-0469(1990)047<1417:OTBDOR>2.0.CO;2).
- Chai, J. Y., and G. K. Vallis, 2014: The role of criticality on the horizontal and vertical scales of extratropical eddies in a dry GCM. *J. Atmos. Sci.*, **71**, 2300–2318, <https://doi.org/10.1175/JAS-D-13-0351.1>.
- Chang, E. K. M., 1993: Downstream development of baroclinic waves as inferred from regression analysis. *J. Atmos. Sci.*, **50**, 2038–2053, [https://doi.org/10.1175/1520-0469\(1993\)050<2038:DDOBWA>2.0.CO;2](https://doi.org/10.1175/1520-0469(1993)050<2038:DDOBWA>2.0.CO;2).
- Chang, E. K. M., and I. Orlanski, 1993: On the dynamics of a storm track. *J. Atmos. Sci.*, **50**, 999–1015, [https://doi.org/10.1175/1520-0469\(1993\)050<0999:OTDOAS>2.0.CO;2](https://doi.org/10.1175/1520-0469(1993)050<0999:OTDOAS>2.0.CO;2).
- Chapman, C. C., A. M. Hogg, A. E. Kiss, and S. R. Rintoul, 2015: The dynamics of southern ocean storm tracks. *J. Phys. Oceanogr.*, **45**, 884–903, <https://doi.org/10.1175/JPO-D-14-0075.1>.
- Charney, J. G., 1947: The dynamics of long waves in a baroclinic westerly current. *J. Meteor.*, **4**, 136–162, [https://doi.org/10.1175/1520-0469\(1947\)004<0136:TDOLWI>2.0.CO;2](https://doi.org/10.1175/1520-0469(1947)004<0136:TDOLWI>2.0.CO;2).
- Charney, J. G., and P. G. Drazin, 1961: Propagation of planetary-scale disturbances from the lower into the upper atmosphere. *J. Geophys. Res.*, **66**, 83–109, <https://doi.org/10.1029/JZ066i001p00083>.
- Deng, Y., and M. Mak, 2006: Nature of the differences in the intraseasonal variability of the Pacific and Atlantic storm tracks: A diagnostic study. *J. Atmos. Sci.*, **63**, 2602–2615, <https://doi.org/10.1175/JAS3749.1>.
- Dickinson, R. E., 1969: Theory of planetary wave-zonal flow interaction. *J. Atmos. Sci.*, **26**, 73–81, [https://doi.org/10.1175/1520-0469\(1969\)026<0073:TOPWZF>2.0.CO;2](https://doi.org/10.1175/1520-0469(1969)026<0073:TOPWZF>2.0.CO;2).
- Edmon, H. J., Jr., B. J. Hoskins, and M. E. McIntyre, 1980: Eliassen-palm cross sections for the troposphere. *J. Atmos. Sci.*, **37**, 2600–2616, [https://doi.org/10.1175/1520-0469\(1980\)037<2600:EPCSFT>2.0.CO;2](https://doi.org/10.1175/1520-0469(1980)037<2600:EPCSFT>2.0.CO;2).
- Farrell, B. F., 1982: Pulse asymptotics of the Charney Baroclinic instability problem. *J. Atmos. Sci.*, **39**, 507–517, [https://doi.org/10.1175/1520-0469\(1982\)039<0507:PAOTCB>2.0.CO;2](https://doi.org/10.1175/1520-0469(1982)039<0507:PAOTCB>2.0.CO;2).
- Fels, S. B., and R. S. Lindzen, 1973: The interaction of thermally excited gravity waves with mean flows. *Geophys. Fluid Dyn.*, **5**, 211–212, <https://doi.org/10.1080/03091927308236117>.
- Fournier, A., 2002: Atmospheric energetics in the wavelet domain. Part I: Governing equations and interpretation for idealized flows. *J. Atmos. Sci.*, **59**, 1182–1197, [https://doi.org/10.1175/1520-0469\(2002\)059<1182:AETIWD>2.0.CO;2](https://doi.org/10.1175/1520-0469(2002)059<1182:AETIWD>2.0.CO;2).
- Fullmer, J. W. A., 1982: The baroclinic instability of highly structured one-dimensional basic states. *J. Atmos. Sci.*, **39**, 2371–2387, [https://doi.org/10.1175/1520-0469\(1982\)039<2371:TBIOHS>2.0.CO;2](https://doi.org/10.1175/1520-0469(1982)039<2371:TBIOHS>2.0.CO;2).
- Gall, R., 1976a: Structural changes of growing baroclinic waves. *J. Atmos. Sci.*, **33**, 374–390, [https://doi.org/10.1175/1520-0469\(1976\)033<0374:SCGBW>2.0.CO;2](https://doi.org/10.1175/1520-0469(1976)033<0374:SCGBW>2.0.CO;2).
- Gall, R., 1976b: A comparison of linear baroclinic instability theory with the eddy statistics of a general circulation model. *J. Atmos. Sci.*, **33**, 349–373, [https://doi.org/10.1175/1520-0469\(1976\)033<0349:ACOLBI>2.0.CO;2](https://doi.org/10.1175/1520-0469(1976)033<0349:ACOLBI>2.0.CO;2).
- Geisler, J. E., and R. R. Garcia, 1977: Baroclinic instability at long wavelengths on a β -plane. *J. Atmos. Sci.*, **34**, 311–321, [https://doi.org/10.1175/1520-0469\(1977\)034<0311:BIALWO>2.0.CO;2](https://doi.org/10.1175/1520-0469(1977)034<0311:BIALWO>2.0.CO;2).
- Gill, A. E., 1982: *Atmosphere-Ocean Dynamics*. Academic Press, 662 pp.
- Green, J. S. A., 1960: A problem in baroclinic stability. *Quart. J. Roy. Meteor. Soc.*, **86**, 237–251, <https://doi.org/10.1002/qj.49708636813>.
- Green, J. S. A., 1970: Transfer properties of the large-scale eddies and the general circulation of the atmosphere. *Quart. J. Roy. Meteor. Soc.*, **96**, 157–185, <https://doi.org/10.1002/qj.49709640802>.
- Harrison, D. E., and A. R. Robinson, 1978: Energy analysis of open regions of turbulent flows—Mean eddy energetics of a numerical ocean circulation experiment. *Dyn. Atmos. Oceans*, **2**, 185–211, [https://doi.org/10.1016/0377-0265\(78\)90009-X](https://doi.org/10.1016/0377-0265(78)90009-X).
- Held, I. M., 1978: The vertical scale of an unstable baroclinic wave and its importance for eddy heat flux parameterizations. *J. Atmos. Sci.*, **35**, 572–576, [https://doi.org/10.1175/1520-0469\(1978\)035<0572:TVSOAU>2.0.CO;2](https://doi.org/10.1175/1520-0469(1978)035<0572:TVSOAU>2.0.CO;2).
- Holopainen, E. O., 1978: A diagnostic study on the kinetic energy balance of the long-term mean flow and the associated transient fluctuations in the atmosphere. *Geophysica*, **15**, 125–145.
- Hoskins, B. J., and P. J. Valdes, 1990: On the existence of storm-tracks. *J. Atmos. Sci.*, **47**, 1854–1864, [https://doi.org/10.1175/1520-0469\(1990\)047<1854:OTEOST>2.0.CO;2](https://doi.org/10.1175/1520-0469(1990)047<1854:OTEOST>2.0.CO;2).
- Hoskins, B. J., M. E. McIntyre, and A. W. Robertson, 1985: On the use and significance of isentropic potential vorticity maps. *Quart. J. Roy. Meteor. Soc.*, **111**, 877–946, <https://doi.org/10.1002/qj.49711147002>.
- Kao, S.-K., and V. R. Taylor, 1964: Mean kinetic energies of eddy and mean currents in the atmosphere. *J. Geophys. Res.*, **69**, 1037–1049, <https://doi.org/10.1029/JZ069i006p01037>.
- Kuo, H.-L., 1949: Dynamic instability of two-dimensional non-divergent flow in a barotropic atmosphere. *J. Meteor.*, **6**, 105–122, [https://doi.org/10.1175/1520-0469\(1949\)006<0105:DIOTDN>2.0.CO;2](https://doi.org/10.1175/1520-0469(1949)006<0105:DIOTDN>2.0.CO;2).
- Kuo, H.-L., 1952: Three-dimensional disturbances in a baroclinic zonal current. *J. Meteor.*, **9**, 260–278, [https://doi.org/10.1175/1520-0469\(1952\)009<0260:TDDIAB>2.0.CO;2](https://doi.org/10.1175/1520-0469(1952)009<0260:TDDIAB>2.0.CO;2).
- Kuo, H.-L., 1979: Baroclinic instabilities of linear and jet profiles in the atmosphere. *J. Atmos. Sci.*, **36**, 2360–2378, [https://doi.org/10.1175/1520-0469\(1979\)036<2360:BIOLAJ>2.0.CO;2](https://doi.org/10.1175/1520-0469(1979)036<2360:BIOLAJ>2.0.CO;2).
- Lapeyre, G., and P. Klein, 2006: Dynamics of the upper oceanic layers in terms of surface quasigeostrophy theory. *J. Phys. Oceanogr.*, **36**, 165–176, <https://doi.org/10.1175/JPO2840.1>.
- Liang, X. S., 2016: Canonical transfer and multiscale energet-

- ics for primitive and quasigeostrophic atmospheres. *J. Atmos. Sci.*, **73**, 4439–4468, <https://doi.org/10.1175/JAS-D-16-0131.1>.
- Liang, X. S., and A. R. Robinson, 2005: Localized multiscale energy and vorticity analysis: I. Fundamentals. *Dyn. Atmos. Oceans*, **38**, 195–230, <https://doi.org/10.1016/j.dynatmoce.2004.12.004>.
- Liang, X. S., and D. G. M. Anderson, 2007: Multiscale window transform. *Multiscale Model. Simul.*, **6**, 437–467.
- Liang, X. S., and A. R. Robinson, 2007: Localized multi-scale energy and vorticity analysis: II. Finite-amplitude instability theory and validation. *Dyn. Atmos. Oceans*, **44**, 51–76, <https://doi.org/10.1016/j.dynatmoce.2007.04.001>.
- Liang, X. S., and L. Wang, 2018: The cyclogenesis and decay of typhoon damrey. *Coastal Environment, Disaster, and Infrastructure*, X. S. Liang and Y.Z. Zhang, Eds., IntechOpen, <https://doi.org/10.5772/intechopen.80018>.
- Lindzen, R. S., and B. Farrell, 1980: A simple approximate result for the maximum growth rate of baroclinic instabilities. *J. Atmos. Sci.*, **37**, 1648–1654, [https://doi.org/10.1175/1520-0469\(1980\)037<1648:ASARFT>2.0.CO;2](https://doi.org/10.1175/1520-0469(1980)037<1648:ASARFT>2.0.CO;2).
- Lorenz, E. N., 1955: Available potential energy and the maintenance of the general circulation. *Tellus*, **7**, 157–167, <https://doi.org/10.1111/j.2153-3490.1955.tb01148.x>.
- Lorenz, E. N., 1967: *The Nature and Theory of the General Circulation of the Atmosphere*. World Meteorological Organization, 161 pp.
- McWilliams, J. C., and J. M. Restrepo, 1999: The wave-driven ocean circulation. *J. Phys. Oceanogr.*, **29**, 2523–2540, [https://doi.org/10.1175/1520-0485\(1999\)029<2523:TWDOC>2.0.CO;2](https://doi.org/10.1175/1520-0485(1999)029<2523:TWDOC>2.0.CO;2).
- Miles, J. W., 1964: A note on Charney's model of zonal-wind instability. *J. Atmos. Sci.*, **21**, 451–452, [https://doi.org/10.1175/1520-0469\(1964\)021<0451:ANOCMO>2.0.CO;2](https://doi.org/10.1175/1520-0469(1964)021<0451:ANOCMO>2.0.CO;2).
- Nakamura, H., 1992: Midwinter suppression of baroclinic wave activity in the Pacific. *J. Atmos. Sci.*, **49**, 1629–1642, [https://doi.org/10.1175/1520-0469\(1992\)049<1629:MSOBWA>2.0.CO;2](https://doi.org/10.1175/1520-0469(1992)049<1629:MSOBWA>2.0.CO;2).
- Orlanski, I., and J. Katzfey, 1991: The life cycle of a cyclone wave in the southern hemisphere. Part I: Eddy energy budget. *J. Atmos. Sci.*, **48**, 1972–1998, [https://doi.org/10.1175/1520-0469\(1991\)048<1972:TLCOAC>2.0.CO;2](https://doi.org/10.1175/1520-0469(1991)048<1972:TLCOAC>2.0.CO;2).
- Pedlosky, J., 1987: *Geophysical Fluid Dynamics*. 2nd ed., Springer-Verlag, 710 pp.
- Pierrehumbert, R. T., and K. L. Swanson, 1995: Baroclinic instability. *Annual Review of Fluid Mechanics*, **27**, 419–467, <https://doi.org/10.1146/annurev.fl.27.010195.002223>.
- Plumb, R. A., 1983: A new look at the energy cycle. *J. Atmos. Sci.*, **40**, 1669–1688, [https://doi.org/10.1175/1520-0469\(1983\)040<1669:ANLATE>2.0.CO;2](https://doi.org/10.1175/1520-0469(1983)040<1669:ANLATE>2.0.CO;2).
- Pope, S. B., 2000: *Turbulent flows*. Cambridge University Press, 806 pp.
- Ragone, F., and G. Badin, 2016: A study of surface semi-geostrophic turbulence: Freely decaying dynamics. *J. Fluid Mech.*, **792**, 740–774, <https://doi.org/10.1017/jfm.2016.116>.
- Simmons, A. J., and B. J. Hoskins, 1978: The life cycles of some nonlinear baroclinic waves. *J. Atmos. Sci.*, **35**, 414–432, [https://doi.org/10.1175/1520-0469\(1978\)035<0414:TLCOSN>2.0.CO;2](https://doi.org/10.1175/1520-0469(1978)035<0414:TLCOSN>2.0.CO;2).
- Simons, T. J., 1972: The nonlinear dynamics of cyclone waves. *J. Atmos. Sci.*, **29**, 38–52, [https://doi.org/10.1175/1520-0469\(1972\)029<0038:TNDOCW>2.0.CO;2](https://doi.org/10.1175/1520-0469(1972)029<0038:TNDOCW>2.0.CO;2).
- Song, R. T., 1971: A numerical study of the three-dimensional structure and energetics of unstable disturbances in zonal currents: Part II. *J. Atmos. Sci.*, **28**, 565–586, [https://doi.org/10.1175/1520-0469\(1971\)028<0565:ANSOTT>2.0.CO;2](https://doi.org/10.1175/1520-0469(1971)028<0565:ANSOTT>2.0.CO;2).
- Trenberth, K. E., 1986: An assessment of the impact of blocking eddies on the zonal flow during a blocking episode using localized Eliassen-Palm flux diagnostics. *J. Atmos. Sci.*, **43**, 2070–2087, [https://doi.org/10.1175/1520-0469\(1986\)043<2070:AAOTIO>2.0.CO;2](https://doi.org/10.1175/1520-0469(1986)043<2070:AAOTIO>2.0.CO;2).
- Vallis, G. K., 2006: *Atmospheric and Oceanic Fluid Dynamics: Fundamentals and Large-Scale Circulation*. Cambridge University Press, 770 pp.
- Yin, J. H., 2002: The peculiar behavior of baroclinic waves during the midwinter suppression of the Pacific storm track. PhD dissertation, University of Washington, 137 pp.
- Zhao, Y.-B., and X. S. Liang, 2018: On the inverse relationship between the boreal wintertime Pacific jet strength and storm-track intensity. *J. Climate*, **31**, 9545–9564, <https://doi.org/10.1175/JCLI-D-18-0043.1>.
- Zhao, Y.-B., X. S. Liang, and J. P. Gan, 2016: Nonlinear multiscale interactions and internal dynamics underlying a typical eddy-shedding event at Luzon Strait. *J. Geophys. Res. Oceans*, **121**, 8208–8229, <https://doi.org/10.1002/2016JC012483>.
- Zhao, Y.-B., X. S. Liang, and W. J. Zhu, 2018: Differences in storm structure and internal dynamics of the two storm source regions over East Asia. *Acta Meteorologica Sinica*, **76**(5), 663–679, <http://dx.doi.org/10.11676/qxxb2018.033>. (in Chinese)